STScI | SPACE TELESCOPE SCIENCE INSTITUTE

Instrument Science Report TEL 2019

A comprehensive approach to HST focal plane geometric calibration

Johannes Sahlmann, Edmund Nelan, Jesse Averbukh, Colin Cox, Matthew Lallo

August 6, 2019

Abstract

We present a new comprehensive approach to the focal plane geometric calibration of the Hubble Space Telescope (HST). This calibration consists in determining the relative locations and orientations of the Fine Guidance Sensors (FGS) and the HST science instruments. It is necessary for efficient operations, e.g. pointing and target acquisitions, and its quality directly affects the astrometric accuracy of archived products. Our approach is new both in how the necessary data are acquired and in their modeling and analysis. We demonstrate the viability and efficiency of the new approach with the help of four seasons of focal plane alignment data taken in Cycles 24 and 25 (April 2017 – October 2018). We uncover a significant scale error ($\sim 7 \cdot 10^{-4}$) in one axis of the operational FGS3 distortion. New alignments of FGS1, FGS2, ACS-WFC, and WFC3-UVIS are determined relative to the reference FGS3. We find that both cameras and FGS1 exhibit a stable offset of ∼150–170 mas relative to the latest previous measurement. The position of FGS2 is offset by ∼400 mas and continues to evolve, in agreement with previous independent findings. The methods and software developed in this work allow us to take full advantage of the unprecedented accuracy of the astrometric reference frame realized by Gaia *and are directly applicable to the focal plane geometric calibration of the James Webb Space Telescope.*

Contents

1 Introduction

This document describes the analysis of HST focal plane alignment data taken in Cycles 24 and 25. The geometric calibration of the focal plane is necessary for science operations and to enhance the astrometric quality of the archived products. The associated processes evolved from pre-launch until Cycle 23 but followed essentially similar observation and analysis principles, which we will refer to as the *traditional scheme*. Starting in Cycle 24, a new way of collecting the data for HST focal plane alignment was implemented, the *new scheme*. A fundamental change that occurred at the same time is the availability of *Gaia* astrometric catalogs, whose unprecedented precision and accuracy represent a very significant improvement over the traditionally used catalogs.

To exploit the data collected in the new scheme, we developed a new data reduction and analysis process. An overview of the new and improved aspects of this work is given below and described in detail in this document:

- Determine the FGS–FGS, FGS–ACS, and FGS–WFC3 alignment with the same dataset, thereby reducing the number of required HST orbits.
- Implement a single streamlined process that limits the need for manual intervention with code implementation in python when possible, under git version control. This includes (a) a python package to automatically retrieve all relevant data of a calibration program from MAST and extract sources with high-precision pixel positions, (b) an automated pipeline to reduce FGS astrometry data, and (c) a collection of python scripts and packages that implement the focal plane alignment determination and generate the products.
- Develop processes and the associated code base that are directly applicable to JWST focal plane alignment. Most of the concepts are applicable to both observatories in the same way. As a consequence, JWST nomenclature is preferred over HST nomenclature when applicable in this document.
- The JWST SIAF python package pysiaf was adapted to support HST Science Instrument Aperture Files (SIAF) and apertures.

2 Coordinate systems and transformations

HST has a Ritchey-Chretian design and images its FOV onto a curved focal surface with a magnification of ∼10 (Burrows 1990, Section 2.2). Pick-off mirrors route sections of the focal surface to the respective science instruments and the guiders. The HST vehicle (V) coordinate system (right-handed, cartesian V_1, V_2, V_3 axes, sometimes referred to as ST-frame) is defined as being fixed to the optical telescope assembly (OTA), see Kennel, H. F. (1976) and ST/CM-07 (1984). The $+V_1$ is pointing from the primary mirror along the optical axis toward the secondary mirror and the perpendicular V_2, V_3 axes are defined by a hole in the OTA main ring as shown in Figure 1 (CSC/TM-82/6045 1987, Appendix A.2). The units of the V frame coordinates are physical, i.e. m or mm.

In flight, the V-frame is defined and realized by one designated FGS. Until its replacement during SM4, the reference was FGS2 and after SM4 the reference was set to FGS3. The HST focal plane alignment is performed in a coordinate system that is tightly linked to the V frame as described below.

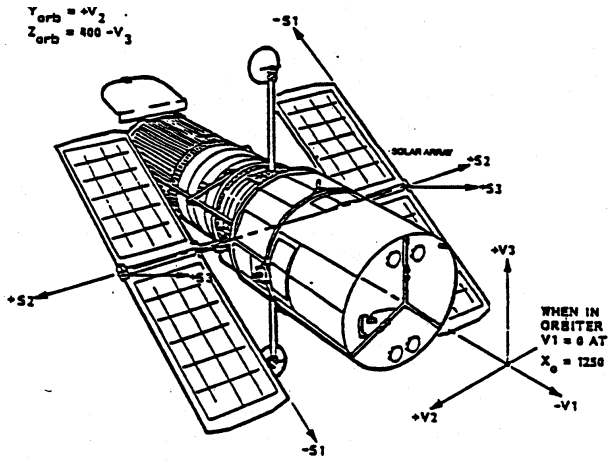

Figure 1: HST observatory V coordinate system definition, from Burrows (1990).

2.1 Idealized focal sphere

We approximate the curved focal surface of HST as an idealized focal sphere. The focal plane alignment is performed in focal sphere coordinates. In this model, HST images a position in the sky onto a position on the focal sphere, and the corresponding transformation can be described by a rotation matrix.

A stellar position in celestial coordinates can be identified by two angles α, δ (i.e. RA, Dec) and the corresponding unit vector (e.g. JWST-PLAN-006166 2016)

$$\hat{\mathbf{w}} = \begin{pmatrix} \cos\alpha\cos\delta \\ \sin\alpha\cos\delta \\ \sin\delta \end{pmatrix}. \tag{1}$$

The object's location on the idealized focal sphere (defined as having unit magnification, i.e. angular separations on the sky and on the idealized focal sphere are equal) can be identified by two Euler angles ν_2, ν_3, where ν_2 is a rotation angle around V_3 and ν_3 is a rotation angle around V_2. The corresponding V-frame unit vector is

$$\hat{\mathbf{w}}' = \begin{pmatrix} \cos\nu_2\cos\nu_3 \\ \sin\nu_2\cos\nu_3 \\ \sin\nu_3 \end{pmatrix} = \begin{pmatrix} V_1 \\ V_2 \\ V_3 \end{pmatrix} = \mathbf{M}\hat{\mathbf{w}} \tag{2}$$

We call the 3D rotation matrix $\mathbf{M}$ that transforms between $\hat{\mathbf{w}}'$ and $\hat{\mathbf{w}}$ the attitude matrix, as defined in Cox & Lallo (2017). The scaling between angular and physical quantities is given by the radius of the focal sphere.

2.1.1 Small angle approximation

In the small angle approximation keeping only the leading term in the Taylor expansion, we have $\sin\nu \approx \nu$ and $\cos\nu \approx 1$, which translates into $V_2 \approx \nu_2$ and $V_3 \approx \nu_3$:

$$\hat{\mathbf{w}}' = \begin{pmatrix} \cos\nu_2 \cos\nu_3 \\ \sin\nu_2 \cos\nu_3 \\ \sin\nu_3 \end{pmatrix} \approx \begin{pmatrix} \sqrt{1-(\nu_2^2+\nu_3^2)} \\ \nu_2 \\ \nu_3 \end{pmatrix} = \begin{pmatrix} \sqrt{1-(V_2^2+V_3^2)} \\ V_2 \\ V_3 \end{pmatrix} \tag{3}$$

For consistency with existing focal plane depictions and because differences are small, we will use V_2,V_3, V_2,V_3, and ν_2,ν_3 interchangeably in the axes labelling of figures.

2.2 Instrument-specific ideal coordinate system

For every instrument aperture, we can define a distortion-free ideal coordinate system with axes X_{idl},Y_{idl},Y_{idl} that are aligned such that the aperture's fiducial point is located on the Z_{idl} axis and the Y_{idl} axis is oriented at an angle V3IdlYangle ('theta' in HST nomenclature) relative to the V_3 axis. A 3D rotation matrix defined by three Euler angles transforms between the ideal and the V-axes or similarly between unit vectors in both coordinate systems. A position at the aperture's fiducial point is characterized by cartesian coordinates $x_{idl}, y_{idl} = 0, 0$ or polar coordinates $\xi, \eta = 0, 0$ on the (now rotated) idealized focal sphere.

A unit vector $\hat{\mathbf{w}}'$ on the idealized focal sphere is transformed to the ideal frame via a 3D rotation matrix $\mathbf{L}$. If the ideal coordinates are planar/cartesian and expressed in units of radians, the corresponding unit vector is

$$\hat{\mathbf{u}} = \mathbf{L}\,\hat{\mathbf{w}}' = \begin{pmatrix} x_{idl} \\ y_{idl} \\ \sqrt{1-(x_{idl}^2+y_{idl}^2)} \end{pmatrix} = \begin{pmatrix} \cos\xi\cos\eta \\ \sin\xi\cos\eta \\ \sin\eta \end{pmatrix}, \tag{4}$$

where we also specified the relationship to the polar angles ξ, η. The rotation matrix $\mathbf{L}$ is a sequence of three rotations around angles given by the V-frame fiducial point V2Ref, V3Ref and the angle V3IdlYangle.

In the planar approximation, these transformations are implemented as shift and rotate operations on two-dimensional coordinates in one single plane (Cox & Lallo 2017).

2.3 Nomenclature

Depending on the observatory and/or the instrument the coordinate systems involved have differing definitions and nomenclature. Table 1 provides an overview of nomenclature for HST and JWST. Table 2 shows a small selection of SIAF fields and their equivalents in both observatories.

2.4 HST FGS coordinate transformations

Vehicle space coordinates of stars observed with the HST FGS are obtained through a series of operations based on the Star Selector Lever Arms and Offsets ([A,B]LEVER, [A,B]OFFST,

Table 1: Coordinate system nomenclature. For HST FGS definitions see Blazek (1984). For JWST definitions see JWST-PLAN-006166 (2016) and Cox & Lallo (2017).

HST FGS		HST camera		JWST	
Name	Unit	Name	Unit	Name	Unit
star-selector/image space	angular	SIDS	pixel	Detector (det)	pixel
distorted Object/FGS space	angular	SIAS	pixel	Science (sci)	pixel
corrected Object/FGS	angular	SICS	angular	Ideal (idl)	angular
ST-frame/Vehicle space	angular	V-frame	angular	V-frame (tel)	angular

Table 2: SIAF field names for HST and JWST.

HST	JWST
SI_mne	InstrName
ap_name	AperName
a_shape	AperShape
im_par	VIdlParity
theta	V3IdlYAngle
a_v2_ref	V2Ref
a_v3_ref	V3Ref
xa0	XSciRef
ya0	YSciRef
ideg	Sci2IdlDeg

2 parameters per A,B star selector and FGS). The first operation transforms star selector encoder values to distorted object space X,Y, which also includes the instantaneous FOV coordinates from the fringe parameters.

The next transformation consists in applying a 2D polynomial transformation to correct for distortion.The polynomial has 11 coefficients and goes up to exponent 5 in both X and Y. This transforms from distorted star positions to undistorted star positions in object space (Luchetti et al. 1988, page 98), (CSC/TM-82/6045 1987, Section 4.2.3). The final step consists in applying the 3x3 TVS alignment matrix (Section 2.4.1) to a 3D unit vector in object space and transform to vehicle space. The effects of differential velocity aberration (DVA) can be corrected in object space (CSC/TM-82/6045 1987, Section 4.2.3), but we chose an implementation where the correction is done on V-frame coordinates, see Section 5.2.

2.4.1 TVS matrix formalism

A TVS matrix is a 3x3 rotation matrix that converts a unit vector from FGS object space into vehicle space. The term 'TVS matrix' probably traces down to CSC/TM-82/6045 (Appendix page A-15, 1987), where matrices transforming from FGS object space to ST vehicle space are named $T_{V/S}$. Sometimes it is referred to as 'FGS (mis-)alignment matrix'. There is one TVS matrix per FGS and in the ideal case it has three nonzero elements of unit value. Because of misalignments, in practice all elements are nonzero and deviate slightly from their ideal values.

The input for the TVS matrix ($\mathbf{M}_{\mathrm{TVS}}$) transformation is a unit vector $\hat{\mathbf{u}}_{\mathrm{idl}}$ obtained on

the basis of cartesian X, Y coordinates in FGS object space[1]:

$$\hat{\mathbf{u}}_{\rm idl} = \begin{pmatrix} X_{\rm idl} \\ Y_{\rm idl} \\ \sqrt{1 - X_{\rm idl}^2 - Y_{\rm idl}^2)} \end{pmatrix} = \begin{pmatrix} \sin(\rho/M)\cos\phi \\ \sin(\rho/M)\sin\phi \\ \cos(\rho/M) \end{pmatrix}, \tag{5}$$

where ρ is the polar radius, M is the magnification, and ϕ is the polar angle (FGS frame LOS vector, CSC/TM-82/6045 1987, Section 4.1.2.2.4) and (FGS star vector in object space, CSC/TM-82/6045 1987, Section 4.2.3.3.3). FGS object space coordinates have their origin on the $V_1 = Z_{\rm idl}$ axis (Blazek 1984, Fig. 1-1) and their fiducial positions are close to $X_{\rm idl} = 0''$, $Y_{\rm idl} = 730''$ for all three FGS[2]. This is fundamentally different from the HST SICS and JWST ideal frame definitions, which have their origins at the fiducial point. For HST FGS, the TVS matrices essentially implement the rotations to place the fiducial points at approximately $\nu_2, \nu_3 = (730, 0)$ for FGS1, (0, -730) for FGS2, and (-730, 0) for FGS3. The center of rotation for the TVS angle parameter is the boresight $\nu_2, \nu_3 = (0, 0)$, which will become relevant in the analysis below.

To define the 9 elements of the TVS matrix by three independent parameters, we defined a set of three alignment parameters $\mathrm{V2Ref_{TVS}}$, $\mathrm{V3Ref_{TVS}}$, $\mathrm{V3Angle_{TVS}}$ per FGS with which we achieve the same behavior as for camera aperture. For example, an offset of $+1''$ in $\mathrm{V2Ref_{TVS}}$ results in an $+\nu_2$ offset by the same amount for FGS1, FGS2, and FGS3 as shown in Figure 2. Similarly, we ensured that an offset in $\mathrm{V3Angle_{TVS}}$ rotates an FGS aperture footprint in the same direction as a camera aperture. The conversion between these three parameters (given in Table 3) and the 9 TVS matrix elements is exact and consists in a series of trigonometric and matrix operations and is implemented in the `pysiaf.HstAperture._tvs_parameters` method. With this description, we can treat an FGS aperture in the same way as a camera aperture, which greatly simplifies our procedures.

In practice, the FGS object space coordinates have been corrected for distortion and differential velocity aberration. The vehicle space unit vector is then obtained by applying the TVS matrix:

$$\hat{\mathbf{v}} = \mathbf{M}_{\rm TVS}\hat{\mathbf{u}}_{\rm idl} = \begin{pmatrix} V_1 \\ V_2 \\ V_3 \end{pmatrix}, \tag{6}$$

where the cartesian vehicle space coordinates constitute the components of the output unit vector $\hat{\mathbf{v}}$. The corresponding polar angles ν_2, ν_3 can be extracted using the standard formulae[3]

$$\begin{aligned} \nu_2 &= \arctan2(V_2, V_1) \\ \nu_3 &= \arcsin V_3 \end{aligned} \tag{7}$$

The role of the TVS matrix $\mathbf{M}_{\rm TVS}$ is equivalent to the $\mathbf{L}$ matrix in Section 2.2.

2.5 HST camera transformations

For the HST cameras, the transformations are analogous to the JWST description given in Cox & Lallo (2017) and implemented in the pysiaf package. Detector pixel coordinates

[1] This is also the way it is being used in the Fortran routine `fgs_to_veh` on line 496.

[2] This is probably because FGS2 is the historic reference guider.

[3] See also an example in `file:/grp/hst/OTA/alignment/14035/Visit1/acs_1.rep`

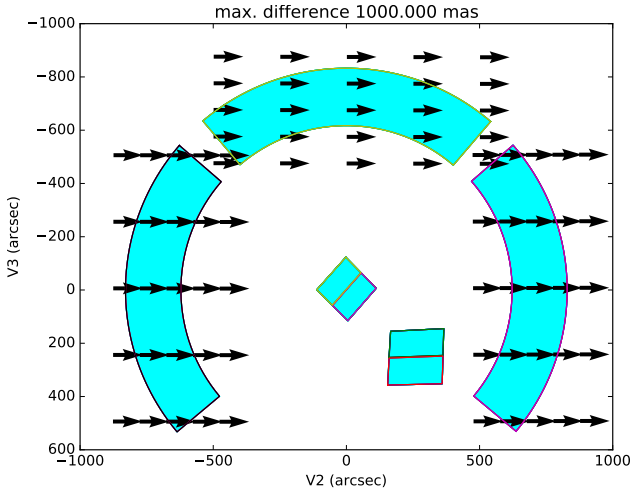

Figure 2: Offsets introduced by converting a regular grid of FGS1, FGS2, FGS3 ideal coordinates with the nominal alignment parameters and with $\mathrm{V2Ref_{TVS}}$ $+1''$. All arrows have an amplitude of $1''$.

Table 3: FGS alignment parameters defined to be equivalent to camera alignment parameters. These correspond to the TVS matrices in `amu.rep` version 1.11.

Aperture	$\mathrm{V2Ref_{TVS}}$ ($''$)	$\mathrm{V3Ref_{TVS}}$ ($''$)	$\mathrm{V3Angle_{TVS}}$ (deg)	($''$)
FGS1	-4.546	-7.160	0.205685	740.465
FGS2	-0.222	5.346	-0.127217	-457.982
FGS3	4.677	-6.181	-0.118065	-425.034

in SIDS are transformed to aperture coordinates (science frame, SIAS), then distortion-corrected (including scale) into the corrected frame (SICS, ideal frame), and finally transformed to vehicle space (V frame).

2.6 Exact and approximate transformations: planar versus spherical models

Historically, the quality of the astrometric reference catalogs slightly better than one arcsecond combined with the HST field of view size and the operational requirements on the focal plane geometric calibration meant that the choice of using accurate spherical transformation or planar approximations had little effect on the results. Now, with the availability of *Gaia* high-precision astrometric catalogs and with the more stringent requirements of JWST in mind, we followed a different approach in which we defined a rigorous model aimed at using exact transformations and call out approximations explicitly. The analysis code was written in a way that allows the user to switch between rigorous and approximate treatments, which allows us to determine the effect on the results.

2.6.1 Transformations between stellar coordinates and the V frame

The attitude matrix formalism (Eq. 2) is exact, but approximations can implicitly be made depending on how the V-frame unit vector components are used. The difference between using V_2, V_3 or ν_2, ν_3 (from Eq. 7) across the HST FOV is shown in Fig. 3. At the edge of the field differences amount to several mas, thus are no longer negligible. For the `rotations` module of the `pysiaf` package, the inputs and outputs of the `pointing` and `getv2v3` functions are ν_2, ν_3.

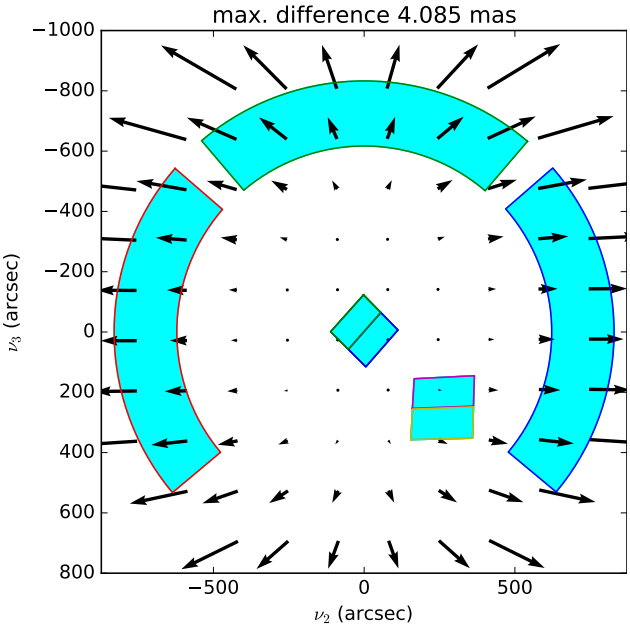

Figure 3: Difference between using V_2, V_3 or ν_2, ν_3 across the HST FOV. To produce the figure, we generated a regular grid of cartesian FGS object space coordinates $(X_{\rm idl}, Y_{\rm idl})$ and transformed them using the TVS matrix of FGS1. The length of the longest arrow is indicated in the figure title.

2.6.2 Transformations between the V frame and the ideal frame (or FGS object space)

For camera apertures, the default JWST SIAF transformations between ideal and V frame are performed in the planar approximation, i.e. transforming between two sets of cartesian coordinates on the same two-dimensional plane using shift and rotate operations (Cox & Lallo 2017, Section 4.3). For the HST camera apertures the same approximation can be applied. However, we also implemented the 3D spherical transformation using Eq. 4.

For FGS apertures, the spherical TVS matrix transformation is always used as described in Section 2.4.1 and the ideal frame coordinates are always assumed to be cartesian (see Section 4.1). Hence, there is no difference between spherical and planar models for this specific FGS transformation.

2.6.3 Transformations between the ideal frame and science pixel frame

The transformations between the camera science and ideal frames (distorted and undistorted object space for FGS) are supposed to account for distortion and scale and are implemented as bivariate (two-dimensional) polynomials (e.g. Sahlmann 2017). Implicit or explicit approximations can be made when treating ideal frame coordinates as cartesian or spherical (Section 2.2), which corresponds to determining whether the distortion coefficients account for tangent-plane projection effects, e.g. gnomonic projection (Calabretta & Greisen 2002, Sect. 5.1.3) or not.

2.6.4 Comparison of the *planar* and *spherical* treatments

The focal plane alignment procedures involve numerous (consequent) transformations between the various frames, where alignment parameters are adjusted iteratively. Tables 4 and 5 summarize the input and output coordinate types in the different cases.

Table 4: Transformations in the planar approximation case. Typically used units are indicates in parenthesis.

Aperture	Input	From frame	Transformation	To Frame	Output
Camera	Cartesian (pixel)	Science	`sci_to_idl`	Ideal	Cartesian (″)
Camera	Cartesian (″)	Ideal	`idl_to_sci`	Science	Cartesian (pixel)
Camera	Cartesian (″)	Ideal	`idl_to_tel`	V-frame	Cartesian (″)
Camera	Cartesian (″)	V-frame	`tel_to_idl`	Ideal	Cartesian (″)
FGS	Cartesian (″)	Ideal	`idl_to_tel`	V-frame	Cartesian (″)
FGS	Cartesian (″)	V-frame	`tel_to_idl`	Ideal	Cartesian (″)
Any	Polar (deg)	Sky	`getv2v3`	V-frame	Cartesian (″)
Any	Cartesian (″)	V-frame	`pointing`	Sky	Polar (deg)

Table 5: Transformations in the spherical treatment case. Typically used units are indicates in parenthesis.

Aperture	Input	From frame	Transformation	To Frame	Output
Camera	Cartesian (pixel)	Science	`sci_to_idl`	Ideal	Polar (″)
Camera	Polar (″)	Ideal	`idl_to_sci`	Science	Cartesian (pixel)
Camera	Polar (″)	Ideal	`idl_to_tel`	V-frame	Polar (″)
Camera	Polar (″)	V-frame	`tel_to_idl`	Ideal	Polar (″)
FGS	Cartesian (″)	Ideal	`idl_to_tel`	V-frame	Polar (″)
FGS	Polar (″)	V-frame	`tel_to_idl`	Ideal	Cartesian (″)
Any	Polar (deg)	Sky	`getv2v3`	V-frame	Polar (″)
Any	Polar (″)	V-frame	`pointing`	Sky	Polar (deg)

3 Calibration principles and history

3.1 Target

The target field was and remains the open cluster M35 (NGC 2168) at a distance of roughly 900 pc (Cantat-Gaudin et al. 2018). M35 has been used since the start of the HST mission for FGS distortion and focal plane calibrations (e.g. McArthur et al. 2006).

3.2 Traditional observation and analysis scheme

In the traditional scheme, the FGS–SI and the FGS–FGS alignment are performed with data collected with independent observations and programs (Abramowicz-Reed 1984).

3.2.1 FGS–SI alignments

Traditional SI–FGS alignment programs since 2009 (starting with 11878) have executed, twice yearly, from SM4 until 2016. The routine programs (e.g. 13616) used 2 HST orbits per epoch (4 orbits per Cycle) and obtained exposures of STIS, ACS, WFC3 and COS while FGS1 and FGS3 were guiding (Cox & Lallo 2010). Resulting locations of the SIs visualized with respect to their SIAF locations can be found at `/grp/hst/OTA/alignment/FocalPlane.xlsx`.

In terms of analysis process and division of labor, STScI performed the observations, analyzed the image data, calculated the results with the help of the GSFC input described below, and generated and delivered the updated SIAF product to the operational database (SCIOPSDB) when needed. No products resulting from an SI update are known or utilized by GSFC/STOCC. The GSFC Sensor Calibration group (SAC) provided to STScI a refined attitude estimation on the basis of the two guide stars[4]. This allowed STScI to compute the V2,V3 coordinates for the RA,Dec stellar positions of stars located in pixel space. The comparison of expected and actual V2,V3 coordinates allowed STScI to determine the new SI locations. Because of the small number of stars typically measured in the cameras, SIAF updates (if any) were usually restricted to the fiducial point positions and updates to the rotation were neither computed nor made.

The principle of these FGS-SI alignment is that the mapping of SI location in vehicle space is determined only via one single set of two guide stars in FGS1 and FGS3 (the same guide star pair is used for both orbits in one epoch). This therefore neglects any potential misalignments of FGS1 and FGS3 relative to the reference FGS. The data collected in this way were relatively noisy due to uncalibrated FGS evolution, proper motion and position errors, and the small number of extracted sources in the apertures. As a result of measured alignment evolution, SIAF updates (`http://prd.stsci.edu/prd/sciopsdb/siaf/siaf_install.htm`) to the locations of the SIs have not been performed since late 2011.

[4]A standard tool (*SI-FGS Report tool*) is utilized by the SAC to do this. STScI has successfully reproduced this tool in the past (e.g. findtarget.f). It was last used in support of SM4, and reproduced the SAC results. This tool was not not used in this work.

3.2.2 FGS–FGS alignments

The FGS-FGS alignment procedure was originally designed in the following way: *For the intermediate solution, stars are observed in the three FGSs simultaneously. FGS2 is the fiducial and its field of view is extended to encompass the remaining FGSs. The star vectors as seen in the extended FGS2, the star vectors as actually measured in each FGS, and the angular separations computed from ground measurements are used to calculate relative alignments of FGS3 with respect to FGS2, and FGS1 with respect to FGS2. The algorithms consist of least-squares techniques for extending the field of view of FGS2 and the q method for determining the rotation matrices* (Abramowicz-Reed 1984; Bradley et al. 1991). The original FGS-FGS and FGS-SI alignment procedures are also described in CSC/TM-82/6045 (1987, Section 4.2.5), which details the process of performing computations in FGS object space coordinates, using the vehicle space to compare FGS–FGS and FGS–SI coordinates, and using rotation matrix solvers to find the alignment parameters. The q method is one way of estimating the optimal 3D rotation matrix that transforms one set of coordinates into a second set and is often used for attitude determination. Other methods, such as singular value decomposition (SVD), exist with often negligible differences in accuracy and efficiency (Markley & Mortari 2000).

FGS-FGS alignments have been performed via separate observations and since SM4, FGS updates have been made in 2011, 2013 (13173, 30 orbits, all three FGS), and 2016 (14457, 5 orbits, FGS2 only). These included the FGS-FGS alignment and the recalibration of geometric distortion coefficients (Optical Field Angle Distortion, OFAD). For these programs, STScI performed the observations and supplied all applicable catalog astrometry to the GSFC SAC who then obtained and processed the FGS data, calculated the results, and generated and delivered to STScI the applicable FGS products described in Section 3.4. FGS misalignments were determined by using the observed and catalog star positions as input to the SAC program OTACAL to compute the alignment correction. A weighted comparison of the observed star separations and the equivalent reference star separations is used to compute an alignment correction relative to a selected standard sensor (Kimmer 2015).

These observations consisted in obtaining astrometry of a sample (10–20 per orbit) of stars with one FGS while the other two FGSs were executing the guide functions on two defined guide stars. This was repeated for five orbits with a different pair of guide stars in each orbit. No SI data were taken. The principle of these FGS-FGS alignments is therefore that the position of a guiding FGS relative to the astrometry FGS can be constrained on the basis of the 5 guide stars and the repeatedly observed stars in the astrometry FGS.

3.3 Principles of the new scheme

In the new FGS-SI alignment scheme, we obtain ACS and WFC3 imaging in parallel with position mode (POS) astrometry in the non-guiding FGS. During a three-orbit sequence at a given epoch each of FGS1, FGS2, and FGS3 perform the astrometry function in turn. Figure 4 illustrates this for FGS2 as the astrometer. This allows direct measurement of the location of the imaging apertures relative to the astrometer FGS using up to ∼20 stars in the FGS, providing knowledge of scale, rotation, and translation of that FGS, which can not

be separately obtained from only one guide star pair.

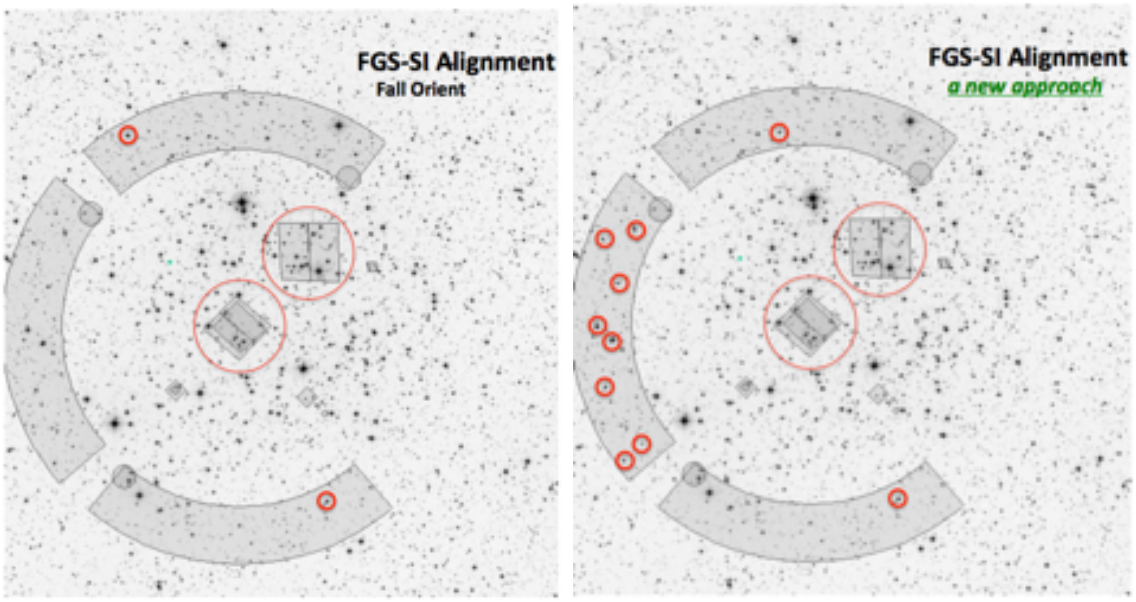

Figure 4: Illustration of the relevant HST instrument apertures in the M35 field. *Left:* Traditional scheme: SI data is taken with two guide stars providing the link to vehicle space. *Right:* New scheme: WFC3 and ACS images are taking images in parallel with FGS2 astrometry of several stars.

The data collected in this way also allow us to determine the relative FGS–FGS locations by means of the SI images to compare the locations of FGS apertures and camera apertures. In principle, this should allow for higher-accuracy in the FGS-FGS calibration because more stars are available in each FGS (between 11 and 19 in the new scheme as compared to 5 in the traditional scheme). It is one of the purposes of this study to establish the quality of the FGS-FGS alignment determined through a process that simultaneously solves for both the SI-FGS and FGS-FGS alignments.

3.4 Calibration products

The (non-exhaustive) list of main focal plane calibration products is given below:

- For SI evolution, the SIAF records and cgg5 table (which contains the full history of a subset of the SIAF elements) are updated in the HST SCIOPSDB SIAF, e.g. `siaf.dat`[5].
- For FGS evolution, the products are installed in the HST SCIOPSDB and described at the HST SCIOPSDB FGS update page (http://prd.stsci.edu/prd/sciopsdb/fgs/index.htm). These products include TVS matrices captured in `amu.rep`[6].

[5] http://prd.stsci.edu/prd/sciopsdb/uvm/UVMelem.cgi?ELEM=sdb/siaf.dat&REV=Latest
[6] http://prd.stsci.edu/prd/sciopsdb/uvm/UVMelem.cgi?ELEM=tooldat%2Famu.rep&REV=Latest

- FGS distortion coefficients: Image space distorted-to-true coefficients are located in schf.dat (search for 'OPTCOF'). There are only 11 nonzero coefficients in these tables corresponding to the polynomial specified by Luchetti et al. (1988, page 98), whereas the OFAD model of McArthur et al. 2006 has 16 coefficients.

- The HST camera distortion coefficients that we used are stored in the HST SIAF, i.e. we do not use instrument-specific IDCTAB products.

4 Data reduction and source extraction

For a given program, all necessary data is downloaded from MAST using the python code hosted at `https://grit.stsci.edu/ins-tel/hst_fpa_data_preparation`. The data are processed as described below and a standardized data file containing the source position and auxiliary information is produced for every exposure. Only those standardized files are utilized in the downstream processing.

4.1 FGS

The FGS POS mode astrometry observations consist of a sequence of exposures, with each exposure measuring the position of a single specific target star. The exposure sequence is specified in APT to be a 'Sequence Non-INT' which contains two 'Prime + Parallel Group' entries. The FGS is the prime instrument, WFC3-UVIS and ACS-WFC are the 'coordinated parallel' instruments. The first 'Prime + Parallel Group' begins with 'deep' 5.0 second WFC3 and ACS exposures executing in parallel with the first FGS exposure of the sequence. The FGS observations within the first group are terminated after 10 to 11 exposures, which allows the camera buffers to be read and cleared, which cannot happen during FGS exposures when FGS is the prime instrument. Once the camera data are processed onto the solid state recorder, the second 'Prime + Parallel Group' executes. This begins with the WFC3 and ACS obtaining 'shallow' 0.5 second exposures with the FGS resuming astrometric exposures. These observations are designed to fit within a single HST orbit, with the guiding FGS maintaining FineLock on the guide stars, as required by the 'Sequence Non-INT' designation.

FGS positions for the astrometry stars and the two guide stars are provided using a modified version of the FGS science calibration pipeline. The appropriate FITS files are downloaded from MAST and converted to the legacy GEIS file formats (using STSDAS strfits). All FGS calibration coefficients (distortion coefficients, star selector encoder conversions) were taken from `/grp/hst/OTA/2016FocalPlaneCal/FGS_Geometry_Products.rtf`. The archived FGS science data for each exposure contains, for all three FGS, the 25 msec (40 Hz) A & B star selector servo angles, the PMT (Photomultiplier Tube) counts from the four photomultiplier tubes, and the flags and status bits (that indicate the search, acquisition and tracking phase of the observation), as well as relevant header keyword values (e.g., MJD, HST position, velocity, roll angle, etc.). These GEIS files are input to the fortran + C hybrid pipeline program 'calfgsA'. Using the flags and status bits the pipeline locates the FineLock data within the file, computes object space (x,y) position of the star for every 25 msec sample. A trimmed mean (that removes 3-sigma outliers) of the (x,y) data is

computed. This is further refined by removing the deviation of the interferometric signal from true null as determined by the PMT counts. The exposure level (x,y) measurement is corrected for differential velocity aberration (DVA) using the JPL Planetary Ephemeris DE405 and the HST state vector from the FGS header file. The correction for geometric distortion (the Optical Field Angle Distortion) is applied. Identical processing over the same sample interval is applied to the guide star data from the two guiding FGS.

A sequence-level correction to remove spacecraft drift and jitter that occurs during the FGS exposure sequence is modeled and applied by using exposure-level changes in the guide star positions, as well as the time series drift of the astrometer FGS itself using the (~ 3) exposures of a selected 'check star' that are interspersed within the sequence. This allows the FGS astrometry gathered over the entire sequence (and the two Prime + Parallel Groups) to be tied to one reference frame.

In summary, the calfgsA yields $X_{\rm idl}, Y_{\rm idl}$ cartesian coordinates in FGS object space that have been corrected for geometric distortion, differential velocity aberration, spacecraft jitter, and spacecraft drift. The spacecraft drift model during the orbit, which is anchored to the first observation, was estimated using check stars that were measured several times, as well as changes to the guide star positions.

4.1.1 FGS target list

The FGS target list contains 64 unique stars. Table 13 lists 58 of those have a pre-computed cross-match in the `gaiadr2.gsc23_best_neighbour` table of the *Gaia* archive[7] (Gaia Collaboration et al. 2018, 2016; Marrese et al. 2019)

4.2 ACS and WFC3

After downloading the pipeline-produced '_flc.fist' and '_spt.fits' files, pixel positions are extracted from each exposure using the fortran code hst1pass, an improved version of the `img2xym` software package (Anderson & King 2006). This routine runs a single pass of source finding and does not perform neighbor subtraction.

We only use the x, y, q columns of the hst1pass output files. The x, y values correspond to SIAS (science frame) pixel coordinates, i.e. they have not been distortion-corrected. The q column indicates the quality of the PSF fit and is used downstream to select the star sample. For the results presented here, we chose a cutoff value of $q < 0.5$, see Fig. 5. hst1pass does not yield positional uncertainties, so we performed an empirical determination of the astrometric accuracy which yielded 7.0 mas and 4.3 mas for 'deep' and 'shallow' exposures, respectively, see Section A.1. We use those values to set the astrometric precision globally for all sources in both axes.

Auxiliary data that are extracted from the FITS headers and added to the standardized file includes information on aperture, instrument settings, pointing, HST position and velocity.

[7] http://gea.esac.esa.int/archive/

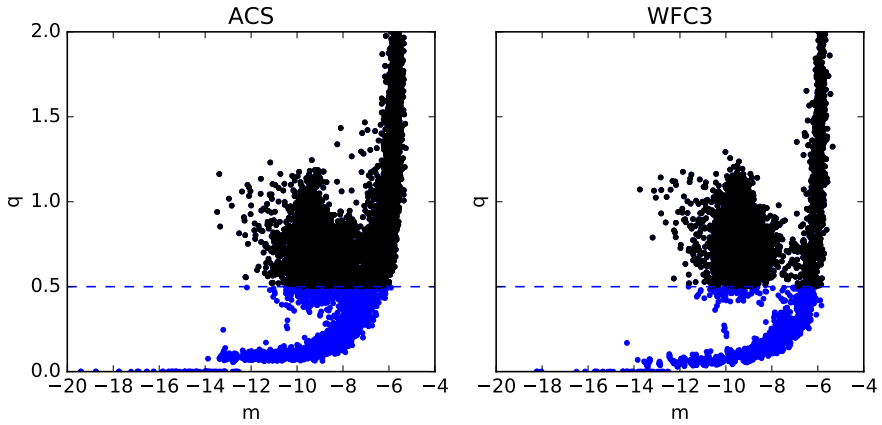

Figure 5: Fit quality indicator q of hst1pass for extracted stars in all processed frames for ACS (*left*) and WFC3 (*right*). Data of both shorter and longer exposures are shown together. The cutoff value of $q = 0.5$ below which the stars are used (blue symbols) is indicated.

4.3 Data summary and characteristics

Four epochs of focal plane alignment data were collected in Cycles 24 and 25 in approximately 6-month intervals. The data consist of FGS astrometry, ACS-WFC F606W images, and WFC3-UVIS F606W images. Consequently, these data do not directly contain SI-FGS alignment information for the COS and STIS instruments.

Table 6 shows a summary of the data collected in Cycles 24 and 25. Every epoch (season) consists of three one-orbit visits. During every visit, we collected one 'shallow' and one 'deep' exposure with ACS and WFC3 while FGS is collecting astrometry of a number of stars sequentially. The table indicates the date, the number of files produced, the exposure time, and the duration which indicates the time span over which the data were acquired. Usually and coherent with the observation design, data were taken over one orbit per FGS. The exception is September 2017 where the data were taken over two consecutive orbits per FGS. This was because the APT file for those observations did not package the two 'Prime + Parallel Group' entries within a 'Sequence Non-INT'. This allowed the scheduling system to break the two groups apart and place them into HST orbits that had smaller visibility windows due to South Atlantic Anomaly (SAA) restrictions. The 'Sequence Non-INT' specification had been applied to all future observations to avoid this fragmentation. Fortunately the September 2017 observations were not degraded by the guide star re-acquisition.

We note that the October 2018 data were obtained just two days before HST entered a safe mode due to gyroscope failure (https://www.nasa.gov/feature/goddard/2018/update-on-the-hubble-space-telescope-safe-mode).

5 Analysis

We describe here the processes as implemented in the new scheme in which we use one HST orbit per FGS and epoch, where the astrometry FGS cycles through stars and WFC3 and ACS take images in parallel. The FGS–SI alignment is directly constrained through the parallel observations, e.g. we determine FGS3–WFC3 alignment when FGS3 is the astrometer

Table 6: Summary of data products for programs 14867 and 15002 as returned from MAST.

program	visit	instrument	start time	N_{files}	exptime (s)	duration (h)	filter
14867	11	ACS/WFC	2017-04-12	2	6.04, 1.56	0.46	F606W
14867	11	FGS	2017-04-12	13	None	0.94	PUPIL
14867	11	WFC3/UVIS	2017-04-12	2	5.00, 0.48	0.49	F606W
14867	12	ACS/WFC	2017-04-12	2	6.01, 1.52	0.45	F606W
14867	12	FGS	2017-04-12	19	None	0.95	F583W
14867	12	WFC3/UVIS	2017-04-12	2	5.00, 0.48	0.47	F606W
14867	13	ACS/WFC	2017-04-12	2	1.53, 6.04	0.48	F606W
14867	13	FGS	2017-04-12	17	None	0.95	PUPIL
14867	13	WFC3/UVIS	2017-04-12	2	0.48, 5.00	0.50	F606W
14867	21	ACS/WFC	2017-09-12	2	6.04, 1.52	1.65	F606W
14867	21	FGS	2017-09-12	17	None	2.12	PUPIL
14867	21	WFC3/UVIS	2017-09-12	2	5.00, 0.48	1.67	F606W
14867	22	ACS/WFC	2017-09-12	2	1.53, 6.04	1.53	F606W
14867	22	FGS	2017-09-12	19	None	2.06	F583W
14867	22	WFC3/UVIS	2017-09-12	2	5.00, 0.48	1.55	F606W
14867	23	ACS/WFC	2017-09-13	2	6.15, 1.53	1.65	F606W
14867	23	FGS	2017-09-13	11	None	2.10	PUPIL
14867	23	WFC3/UVIS	2017-09-13	2	5.00, 0.48	1.67	F606W
15002	11	ACS/WFC	2018-03-19	2	6.19, 1.60	0.46	F606W
15002	11	FGS	2018-03-19	13	None	1.31	PUPIL
15002	11	WFC3/UVIS	2018-03-19	2	5.00, 0.48	0.49	F606W
15002	12	ACS/WFC	2018-03-19	2	1.54, 6.04	0.45	F606W
15002	12	FGS	2018-03-19	19	None	1.38	F583W
15002	12	WFC3/UVIS	2018-03-19	2	5.00, 0.48	0.47	F606W
15002	13	ACS/WFC	2018-03-19	2	1.53, 6.04	0.48	F606W
15002	13	FGS	2018-03-19	17	None	0.95	PUPIL
15002	13	WFC3/UVIS	2018-03-19	2	0.48, 5.00	0.50	F606W
15002	21	ACS/WFC	2018-10-03	2	5.00, 0.51	0.47	F606W
15002	21	FGS	2018-10-03	17	None	0.94	PUPIL
15002	21	WFC3/UVIS	2018-10-03	2	0.48, 5.00	0.49	F606W
15002	22	ACS/WFC	2018-10-04	2	0.51, 5.00	0.41	F606W
15002	22	FGS	2018-10-04	19	None	0.94	F583W
15002	22	WFC3/UVIS	2018-10-04	2	0.48, 5.00	0.43	F606W
15002	23	ACS/WFC	2018-10-04	2	0.51, 5.00	0.51	F606W
15002	23	FGS	2018-10-04	13	None	0.99	PUPIL
15002	23	WFC3/UVIS	2018-10-04	2	5.00, 0.48	0.53	F606W

and we determine FGS2–WFC3 alignment when FGS2 is the astrometer. The FGS–FGS alignment can be indirectly constrained via the camera aperture, i.e. the pair-wise FGS–SI alignments 'link' FGS2 to FGS3 and do constrain the FGS2–FGS3 alignment. The use of parallel/contemporaneous measurements helps to mitigate the effect of attitude errors on the alignment parameters.

5.1 Crossmatch with *Gaia* DR2

The first analysis step is to crossmatch the stars observed in the cameras and the FGS with *Gaia* sources, which define the global reference frame used for focal plane alignment. The

crossmatch is performed in the V-frame. We retrieved all *Gaia* DR2 sources in the vicinity of M35 from the *Gaia* archive (Fig. 6).

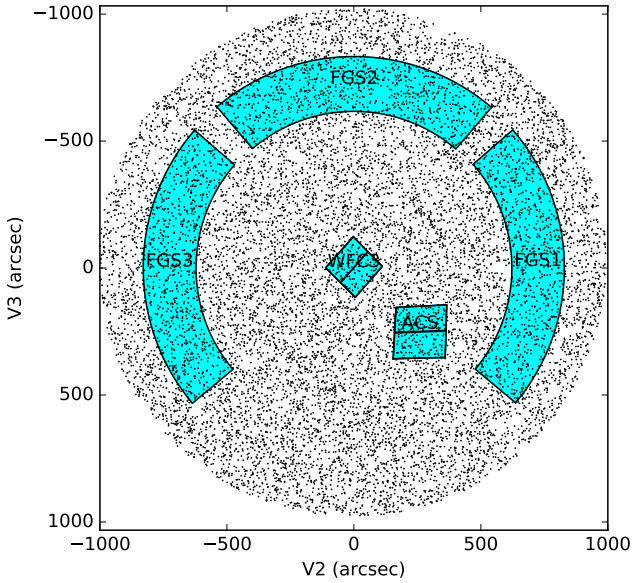

Figure 6: *Gaia* DR2 sources in the M35 field. The relevant HST apertures are shown.

For camera apertures, we applied the cutoff in q value to retain only high-quality measurements before the crossmatch. We used the science frame coordinates from the standardized file to compute ideal and V-frame coordinates on the basis of the operational distortion and alignment coefficients as stored in the HST SIAF. These are standard operations implemented in the pysiaf package, however, WFC3 and ACS science frame coordinates have first to be corrected for 25 and 24 reference pixels in X, respectively, before applying the distortion polynomial. For FGS $X_{\rm idl}, Y_{\rm idl}$ object space coordinates, we apply the operational TVS matrix (from the `amu.rep` file, version 1.11) transformation to the V-frame as described in Section 2.4.1 and implemented in pysiaf.

For every camera and FGS observation, we computed the positions of *Gaia* catalog sources at the epoch given in the FITS header ('EPOCH' keyword) by accounting for proper motion and the relevant covariances to obtain accurate position uncertainties[8]. The *Gaia* equatorial coordinates are transformed to the V-frame using the `pysiaf.rotations` module and the HST attitude as defined by the RA_V1, DEC_V1, and PA_V3 header keywords and the corresponding V-frame coordinate system origin $(\nu_2, \nu_3) = (0, 0)$.

The crossmatch is performed on the basis of the V-frame coordinates of the two sets of observed and *Gaia* catalog stars with a search radius of $1''$. Only crossmatched stars are used for analysis. Table 7 shows the number of sources for FGS3-SI alignment.

One star observed in FGS2 (GSC23 N8CV000450, named FGS2-E-ref6) failed to be cross-identified with *Gaia* and was observed at a reported position $\sim 4''$ off the expected value. Upon inspection of the FGS acquisition scans, this target was identified as a visual binary star which reduced the fringe amplitudes resulting in a failed lock, thus unsuccessful acquisition (Figure 7).

[8]This was implemented with an early and modified version of the gaia package (Price-Whelan 2018).

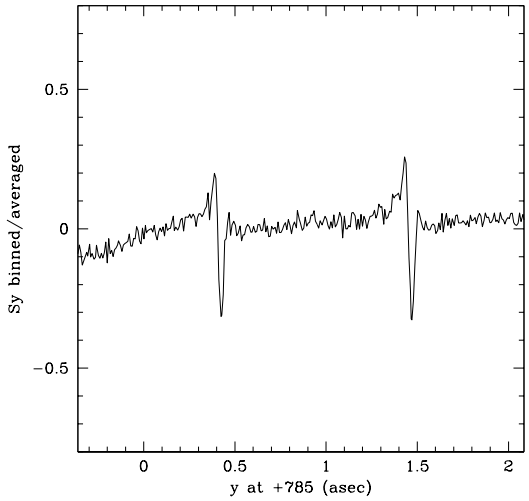

Figure 7: Acquisition scans in the x axis by FGS2 of the target N8CV000450/FGS2-E-ref6. The target is a visual binary as revealed by the second feature.

5.2 Correction of differential velocity aberration

The DVA corrections (e.g. Cox & Gilliland 2003; Cox 1997) are applied to V-frame coordinates and are implemented with calls to a fortran interface to C code with a parameter file (Fig. 8) and list of V-frame coordinates as inputs. The necessary parameter files are prepared in advance and attached to every individual observation. For camera observations, the computation is performed at runtime when transforming from ideal to V-frame coordinates with pysiaf's `aperture.idl_to_tel` method.

```
3                                PRIMESI (FGS header)
-725.48                          V2Ref (FGS header)
-5.830000000000001               V3Ref (FGS, header)
50.0                             V2APERCE (should be FGSOFFV2)
115.0                            V3APERCE (should be FGSOFFV3)
92.31002701086                   RA_V1 (camera _spt.fits header)
24.34344639553                   DEC_V1 (camera header)
270.013611                       PA_V3 (camera header)
4730.955009399                   POSTNSTX (camera header)
4545.9785798                     POSTNSTY (camera header)
-2187.466454503                  POSTNSTZ (camera header)
-4.222161572564                  VELOCSTX (camera header)
5.700121967999                   VELOCSTY (camera header)
2.714453606983                   VELOCSTZ (camera header)
2017 102 10 36 33.882            EXPSTART (camera header)
```

Figure 8: Example of a DVA correction parameter file.

Table 7: Number of sources used for FGS3-SI alignment. N_a is the number of extracted sources that pass the quality criteria, N_{Gaia} is the number of *Gaia* DR2 sources within the aperture (for guiders this columns shows the unique number of cross-matched sources), $N_{\rm matched}$ is the number of cross-matched sources, and $N_{\rm used}$ is the number of sources used for alignment.

pid_visit	Instr.	Aperture	$T_{\rm exp}$ (s)	N_a	N_{Gaia}	$N_{\rm matched}$	$N_{\rm used}$
14867_13	WFC3	IUVIS2FIX	5.0	57	52	49	45
14867_13	WFC3	IUVIS1FIX	5.0	59	59	50	47
14867_13	ACS	JWFC1FIX	5.0	118	101	93	86
14867_13	ACS	JWFC2FIX	5.0	102	92	80	74
14867_13	WFC3	IUVIS1FIX	0.5	27	59	23	22
14867_13	WFC3	IUVIS2FIX	0.5	21	52	19	17
14867_13	ACS	JWFC1FIX	0.5	47	101	38	36
14867_13	ACS	JWFC2FIX	0.5	50	92	38	37
14867_13	FGS3	FGS3	None	16	12	16	16
14867_13	FGS3	FGS3	None	16	12	16	16
14867_23	WFC3	IUVIS2FIX	5.0	57	58	51	47
14867_23	WFC3	IUVIS1FIX	5.0	63	50	45	40
14867_23	ACS	JWFC1FIX	5.0	104	77	72	68
14867_23	ACS	JWFC2FIX	5.0	103	86	82	74
14867_23	WFC3	IUVIS1FIX	0.5	23	50	17	16
14867_23	WFC3	IUVIS2FIX	0.5	26	58	24	24
14867_23	ACS	JWFC2FIX	0.5	42	86	34	31
14867_23	ACS	JWFC1FIX	0.5	58	77	43	41
14867_23	FGS3	FGS3	None	10	8	10	10
14862_23	FGS3	FGS3	None	10	8	10	10
15002_13	WFC3	IUVIS2FIX	5.0	57	52	51	47
15002_13	WFC3	IUVIS1FIX	5.0	60	59	53	51
15002_13	ACS	JWFC1FIX	5.0	112	101	90	86
15002_13	ACS	JWFC2FIX	5.0	102	92	84	79
15002_13	WFC3	IUVIS1FIX	0.5	26	59	24	23
15002_13	WFC3	IUVIS2FIX	0.5	18	52	17	16
15002_13	ACS	JWFC1FIX	0.5	46	101	38	35
15002_13	ACS	JWFC2FIX	0.5	49	92	38	36
15002_13	FGS3	FGS3	None	16	12	16	16
15002_13	FGS3	FGS3	None	16	12	16	16
15002_23	WFC3	IUVIS2FIX	5.0	62	58	51	45
15002_23	WFC3	IUVIS1FIX	5.0	60	50	46	44
15002_23	ACS	JWFC1FIX	5.0	100	77	74	71
15002_23	ACS	JWFC2FIX	5.0	95	86	75	59
15002_23	WFC3	IUVIS1FIX	0.5	20	50	17	17
15002_23	WFC3	IUVIS2FIX	0.5	29	58	25	25
15002_23	ACS	JWFC2FIX	0.5	39	86	34	31
15002_23	ACS	JWFC1FIX	0.5	51	77	41	39
15002_23	FGS3	FGS3	None	12	9	12	12
15002_23	FGS3	FGS3	None	12	9	12	12

5.3 Determination of relative alignment between apertures, FGS–SI alignment

The relative positions and orientations of camera and FGS apertures are determined in the V-frame. Since the reference for the geometric calibration is defined by the *Gaia* catalog of stellar coordinates and it is the HST attitude that allows us to transform between RA, Dec and V-frame coordinates, the attitude determination is a critical component of the focal plane alignment. This is amplified by the roll-angle component of the attitude which can introduce alignment errors that depend on the radial distance of apertures from the telescope V_1 axis, see Fig. 9. These cannot be mitigated by differential measurements because those can only eliminate constant offsets in the V frame. For the size of the HST focal plane, an $1''$ error in attitude roll angle can translate into a relative position error of $\sim$4 mas at the location of the FGS. The reduce the effect of attitude uncertainty to a minimum we use contemporaneously acquired datasets (parallel observations) as much as possible.

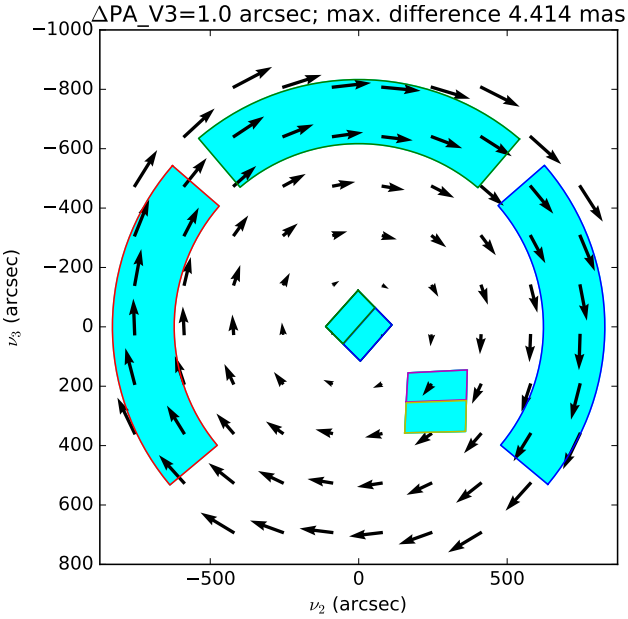

Figure 9: Position differences of stellar coordinates that have been transformed to the V frame with attitudes that differ by $1''$ in roll angle. The length of the longest arrow is indicated in the figure title.

5.3.1 Attitude groups

Since attitude knowledge directly translates into the accuracy of alignment results, we group observations into sets for which we assume that the attitude is constant. Due to the nature of the observations and the quality of the attitude control, this is necessarily an approximation. Here, an 'attitude group' usually comprises observations with 5 apertures that are nearly contemporaneous: two chips of ACS, two chips of WFC3, and the astrometry FGS. Since we took two camera exposures of different depth per orbit, we have two attitude groups per orbit. The FGS observations are duplicated in both groups and were collected over the

full usable orbit duration. The attitude evolution during the sequence of FGS astrometry measurements is partially accounted for with the drift model on the basis of check stars.

5.3.2 Alignment-reference aperture and attitude-defining aperture

Focal plane alignment relies inherently on relative measurements and an alignment-reference aperture has to be defined. Similarly, the V-frame is realized by one reference aperture, which in turn defines the attitude. We call that aperture the attitude-defining aperture. In general, alignment-reference aperture and attitude-defining aperture are identical, by default that would currently be FGS3, but there are scenarios in which they have to be different. These two parameters can therefore be set independently in the analysis.

5.3.3 Fitting a two-dimensional distortion polynomial model

To fit a bivariate distortion polynomial, we use the framework and methods described in Sahlmann (2017) and code hosted at https://grit.stsci.edu/jsahlmann/pystortion.

5.3.4 Attitude determination

During observations under fine guidance, the HST attitude is controlled by the two guiding FGS, where the FGS that controls translational attitude is the dominant guider, and the FGS that controls roll is the subdominant guider (Nelan & Makidon 2002).

A first estimate of the HST attitude can be derived from FITS header information: The RA and Dec of the V_1 axis (RA_V1 and DEC_V1, respectively) and the position angle of the V_3 axis (PA_V3) map to the origin of the V-frame ($\nu_2 = 0, \nu_3 = 0$)=($V_2 = 0, V_3 = 0$), thus determine the initial attitude estimate. More accurate estimations can be made with standard observations[9] but are usually limited to an accuracy of $\sim 0.003^\circ \simeq 11''$[10], which is insufficient for our purposes (see Fig. 9).

We implemented an iterative procedure to refine that first attitude determination. It relies on simultaneously solving for attitude and relative aperture location errors. First we define the set of apertures to be used, typically these are all available apertures because the attitude precision (in particular for the critical roll angle) increases with the size of the field covered and the number of used stars. For the purpose of this step, the attitude-defining aperture also serves as alignment-reference aperture.

The iterations start with the single attitude-defining aperture. We keep the V-frame coordinates of the measured stars in that aperture fixed and use the initial attitude estimate from the FITS header to compute the V-frame coordinates of the crossmatched *Gaia* stars. A first-degree bivariate distortion polynomial which includes offset, scale, and skew parameters (6 free parameters, Section 5.3.3) is used to map both coordinate sets. The linear offset terms and the rotation of the Y-axis extracted from the polynomial coefficients are used to iteratively correct the RA_V1, DEC_V1, and PA_V3 inputs to the current attitude estimate until convergence is reached (typically when the correction is smaller than ϵ times

[9] http://www.stsci.edu/hst/observatory/faqs

[10] http://www.stsci.edu/hst/observatory/pointing/obslog/OL_7.html#HEADING55

the parameter uncertainty, where ϵ is a small number). These iterations are similar to the description in Section 5.4.

Next, we add the aperture from the chosen set of apertures that lies closest in the focal plane and use the current aperture to determine its relative V-frame location using the procedure described in Section 5.4. That step also includes the determination of the aperture-level low-order distortion, which is the residual distortion after correction with the SIAF distortion model. Then we repeat the iterative attitude correction determination as described above which yields an update to the current aperture with smaller uncertainties in its parameters. These steps are repeated until the full set of apertures is used for the attitude determination.

The adjusted parameters in this procedure are the attitude's RA_V1, DEC_V1, and PA_V3, the low-order (residual) distortion coefficients of all used apertures, and the alignment parameters of apertures relative to the attitude-defining aperture. However, the only parameters that are retained for the focal plane alignment determination are the updated RA_V1, DEC_V1, and PA_V3, which define the final attitude determination.

5.4 Determination of relative alignment parameters

In the case of camera to camera alignment, the reference aperture is outlined by an approximate rectangle in the V frame. Its alignment parameters are given by the V2Ref, V3Ref values of the fiducial point and the V3IdlYAngle that defines the position angle of the aperture's ideal Y-axis relative to V_3 and measured about the ideal frame origin. These three parameters are kept at a fixed value (defined at some time of the mission) for the reference aperture, thereby establishing the relationship between stellar coordinates and V-frame coordinates via the observatory attitude.

The determination of relative alignment parameters for a second rectangular aperture involves using an attitude estimation to convert the reference catalogues coordinates to the V frame. Bivariate polynomial models that may include high-order distortion terms can be used to map star images to catalogue entries in the V-frame. The relative alignment parameters can be found by iteratively[11] altering the V2Ref, V3Ref, V3IdlYAngle parameters of the aperture until the offset and Y-angle terms of the corresponding polynomial are negligible. These 'corrections' to the alignment parameter are determined for both the reference and the dependent aperture, because the attitude determination leads to small offsets between the expected and actual position of stars in the reference aperture. The iterative process is illustrated in Figure 10.

We define three sets of alignment parameters $p_{i,\mathrm{current}}$, $p_{i,\mathrm{corrected}}$, and $p_{i,\mathrm{calibrated}}$, where $p \in$[V2Ref, V3Ref, V3IdlYAngle] and the index i indicates the aperture, i.e. one of FGS1, FGS2, FGS3, IUVIS1FIX, IUVIS2FIX, JWFC1FIX, JWFC2FIX. $p_{i,\mathrm{current}}$ is the currently valid value of the parameter, typically that is the values corresponding to the SIAF or TVS parameters in the SCIOPS database. $p_{i,\mathrm{corrected}}$ are the best-fit alignment parameters determined with the procedure above. $p_{i,\mathrm{calibrated}}$ are the adopted new alignment parameters that take into account the relative nature of the measurements:

$$p_{i,\mathrm{calibrated}} = p_{i,\mathrm{corrected}} - (p_{\mathrm{ref,corrected}} - p_{\mathrm{ref,current}}) \qquad \text{for } p \in [\mathrm{V2Ref}, \mathrm{V3Ref}], \tag{8}$$

[11] The need for iterative approaches to such analyses was already established in Luchetti et al. (1988).

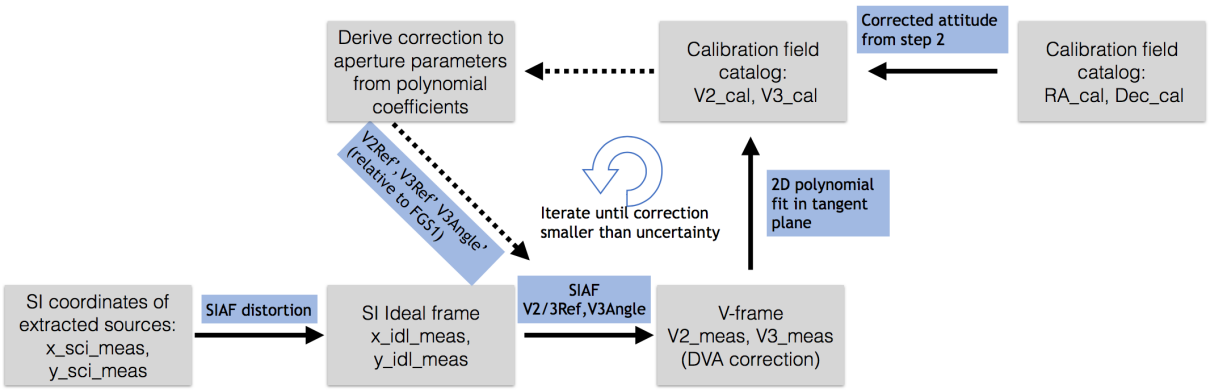

Figure 10: Iterative scheme for determining relative alignment parameters.

where $_{\text{ref}}$ identifies the alignment-reference aperture. Except for the alignment-reference aperture, the calibrated clocking angle is the same as the corrected value, because the effect of a rotation is not constant across the field (as opposed to an offset):

$$\text{V3IdlYAngle}_{i,\text{calibrated}} = \begin{cases} \text{V3IdlYAngle}_{i,\text{current}}, & \text{if } i = \text{ref} \\ \text{V3IdlYAngle}_{i,\text{corrected}}, & \text{else} \end{cases} \tag{9}$$

The TVS formalism for FGS apertures is in principle different, but we defined a set of three alignment parameters $\text{V2Ref}_{\text{TVS}}$, $\text{V3Ref}_{\text{TVS}}$, $\text{V3Angle}_{\text{TVS}}$ per FGS with which we achieve the same behavior as for camera aperture, see Section 2.4.1. With this description, we can treat an FGS aperture in the same way as a camera aperture, which greatly simplifies the procedures.

6 Results

6.1 Alignment of WFC3 and ACS relative to FGS3

When setting FGS3 as the alignment-reference and attitude-defining aperture, we can directly determine the relative location and orientation of WFC3 and ACS for all parallel observations, i.e. for the two exposures taken during one orbit per season (8 measurements in total).

The large FGS3 scale error discussed in Section 6.2 forced us to adapt our analysis as described in Appendix A.2. Here we report only the final results. Figure 11 shows a general overview of our results. Throughout this section we will use the same color coding when displaying the results of all seasons in one panel. The temporal sequence is blue, green, grey, black and shown in Table 8.

Figure 12 shows that all apertures appear shifted by about -150 mas in V_2. Generally, there is good agreement between the four epoch, except for the first epoch in ACS, which appears to be be discrepant at the $\sim$50 mas level. The corresponding V3IdlYangle values usually agree with the SIAF values within $\sim 30''$ and exhibit small variations (Fig. 13). Average offsets of roughly $-13''$ (WFC3) and $-18''$ (ACS) are apparent, see also Table 9.

Table 8: Color coding in Section 6

pid	date	color
14867_1	2017-04-12	blue
14867_2	2017-09-12	green
15002_1	2018-03-19	grey
15002_2	2018-10-03	black

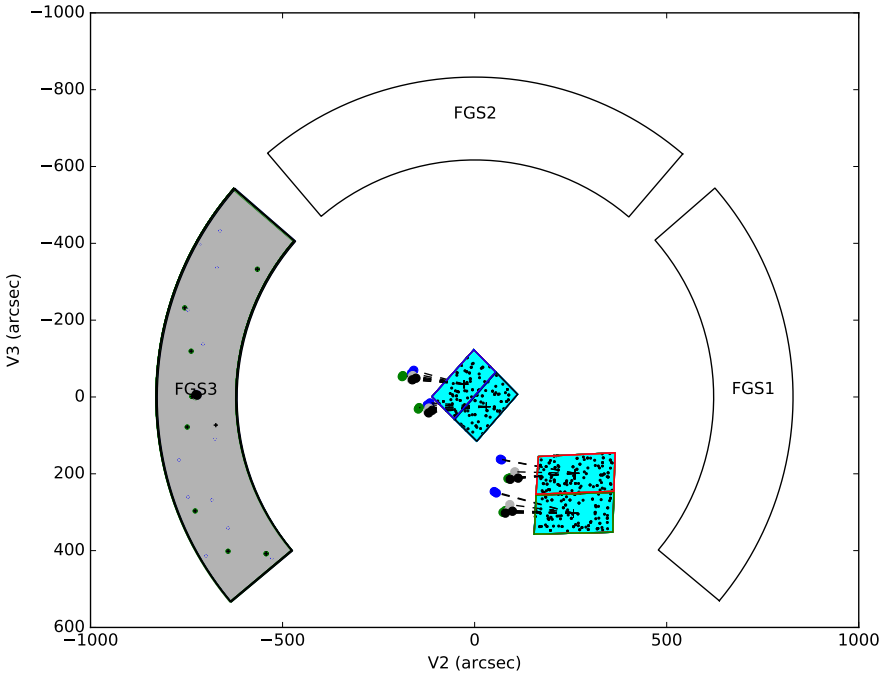

Figure 11: Results of FGS3-SI alignment. The focal plane is shown in the V frame with $+V_3$ pointing down, i.e. FGS1 is to the right, FGS2 is on top, and FGS3 (shaded because it is the reference in this case) is to the left. For each camera chip and exposure, a colored circle with error bar indicates the measured offset relative to the SIAF location, magnified by a factor 1000. Dots within the apertures indicate stars that were used for the alignment. All camera aperture appear to be shifted in $-V_2$ direction.

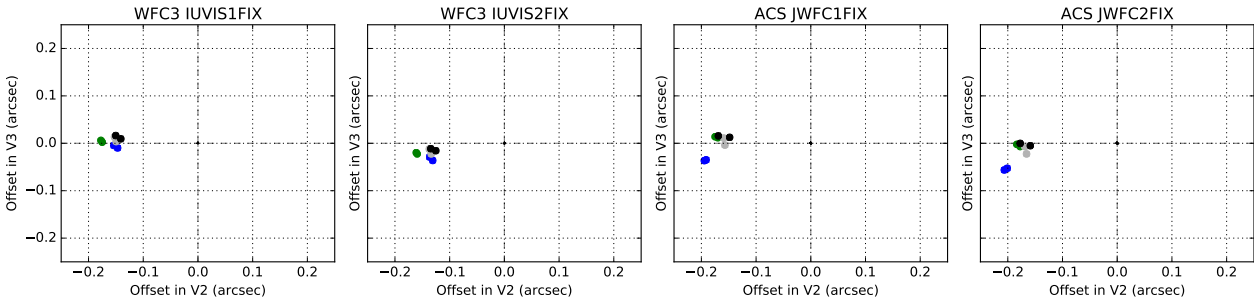

Figure 12: Results of FGS3-SI alignment. The four panels correspond to the four camera chips and the measured offsets relative to the SIAF locations are shown.

We found that the residual distortion terms carry scale terms that differ from unity by $\sim 2 \cdot 10^{-4}$ and $\sim 3 \cdot 10^{-4}$ in V_2 direction for WFC3 and ACS, respectively, and by $\sim 1 \cdot 10^{-4}$ in V_3 direction for ACS (Fig. 14).

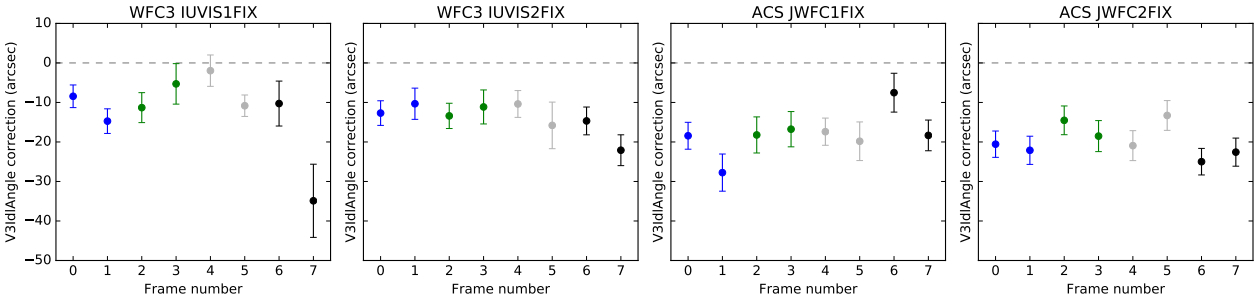

Figure 13: Results of FGS3-SI alignment. The measured angular offsets relative to the SIAF V3IdlYangle values are shown. Note that these indicate local rotations about the aperture fiducial point.

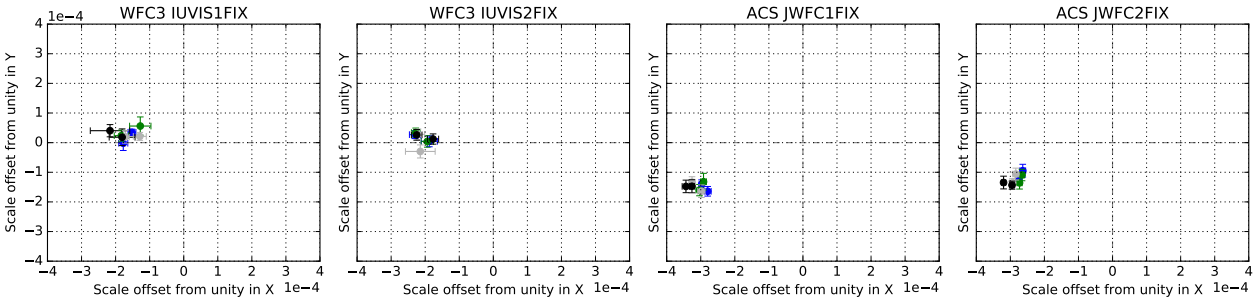

Figure 14: Results of FGS3-SI alignment. These panels show the scale offsets from unity for the camera apertures, where unity refers to the scale at the fiducial point corresponding to the SIAF distortion polynomial.

In Figure 15 we show the historic evolution of the WFC3-UVIS and ACS-WFC alignments. Average offsets of approximately −150 mas (WFC3) and −170 mas (ACS) in V_2 of our measurements relative to the current SIAF is apparent (Table 9), but our measurements are within the typical range of previous determinations. The average discrepancy in V_3 is 20 mas or smaller. Notably, the scatter over two years in our measurements appears significantly smaller than in the historic data. The individual measurements are reported in Tables 15 and 16. Table 9 shows the simple average values in comparison with the current SIAF. The inspection of Figure 16 allows us to estimate the accuracy of our FGS3-SI alignment procedure to ∼10–20 mas[12]. The temporal variations observed over 2 years are a factor of ∼2 larger and it is undefined whether these are actual relative displacements or the effect of inter-season systematic errors.

[12]The two determinations within one orbit are not independent, because they rely on the same FGS dataset. As a consequence the accuracy may be slightly underestimated.

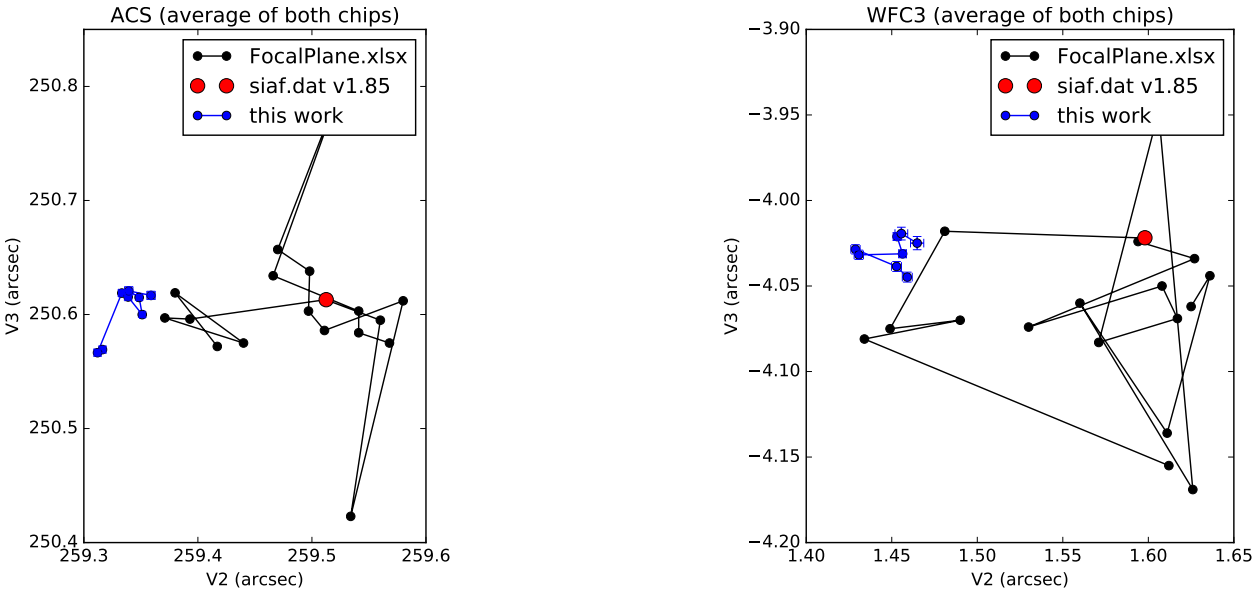

Figure 15: Results of FGS3-SI alignment. The panels compare the camera alignment results of this work (blue symbols) to the previous determinations (black symbols, from /grp/hst/OTA/alignment/FocalPlane.xlsx, latest measurement on 2016-10-02) and the current SIAF values (red circle). The averages of the fiducial locations of both constituting apertures are shown for consistency with the FocalPlane.xlsx data and panel.

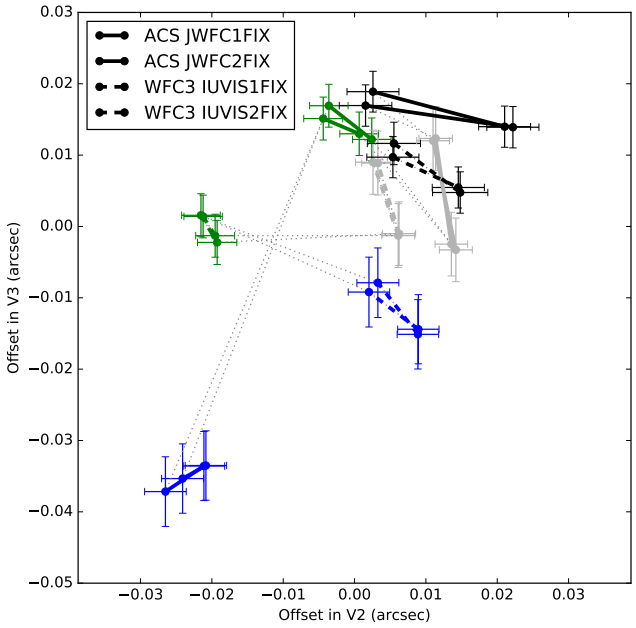

Figure 16: Results of FGS3-SI alignment. This panel shows the mean-subtracted evolution of the four camera chip apertures over the four seasons marked with the usual color-coding. The motions of both chips in a camera are tightly correlated as expected. The typical discrepancies between two determinations during the same orbit (i.e. season) suggest an accuracy of this procedure at the level of ∼10–20 mas.

Table 9: Differences between the average camera positions and the current SIAF.

AperName	V2Ref (arcsec)			V3Ref (arcsec)			V3IdlYAngle (deg)		
	SIAF	this work	difference	SIAF	this work	difference	SIAF	this work	difference (″)
IUVIS1FIX	30.656	30.500	-0.156	25.217	25.221	0.005	44.831	44.828	-12.216
IUVIS2FIX	-27.460	-27.599	-0.140	-33.260	-33.281	-0.021	44.767	44.763	-13.815
JWFC1FIX	261.647	261.476	-0.171	198.665	198.664	-0.001	177.330	177.325	-18.033
JWFC2FIX	257.378	257.198	-0.180	302.561	302.542	-0.019	177.766	177.760	-19.688

6.2 FGS–FGS alignment

The focal plane calibrations of the camera apertures relative to FGS3 presented in the previous section allow us to determine the FGS3–FGS2 and FGS3–FGS1 alignment. To do this, we first apply the camera alignment calibrations by updating the respective aperture attributes (fiducial point coordinates and angle) and then perform a second alignment determination where we set a camera aperture (chip1 of WFC3) as alignment-reference and attitude-defining aperture. The time between the respective datasets is one or two HST orbits, which mitigates the effects of temporal alignment changes and effectively the aligned camera aperture allows us to reference all apertures to the V-frame defining FGS3 aperture.

The attitude determination step in this case is customized to minimize systematic errors in the attitude's position angle as described in Appendix A.3.

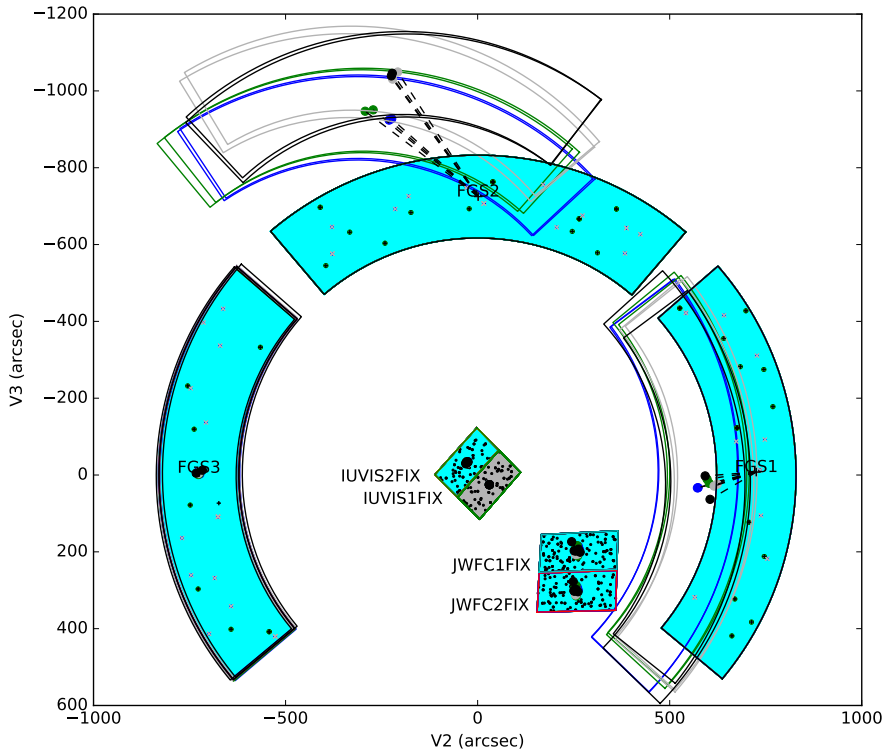

Figure 17: Results of FGS–FGS alignment. The layout is the same as Figure 11, however the reference aperture is now one calibrated camera aperture. For FGS apertures, we show the effect of using the calibrated TVS matrix by drawing the new aperture fiducial point and outline with an offset magnified by a factor 1000. This way of displaying the changes is similar to Kimmer (2015). FGS2 exhibits significant motion in $-V_2$ and $+V_3$ direction, whereas FGS1 appears stable within the uncertainties.

Figure 17 shows the alignment result overview. Figure 18 shows the measured offsets: Since the camera apertures have already been aligned with FGS3, their offsets are close to zero but show a scatter that reflects the procedure's random and systematic errors, in particular the ones caused by attitude determination errors in position angle. Therefore, the scatter increases with radial distance from the reference aperture. In the bottom panels we

show the adjustments to the FGS TVS alignment parameters as defined in Section 2.4.1. These do not map exactly the displacements of the fiducial points shown in Fig. 17, partially because of the change in the rotation origin described in Section A.2. The alignment of FGS3 is maintained as expected. In terms of TVS parameters, FGS1 appears to be misaligned by ∼-150 mas in $-V_2$ direction, whereas FGS2 shows large variations (correlated with the corresponding angle, see Fig. 19) and a misalignment as large as ∼400 mas.

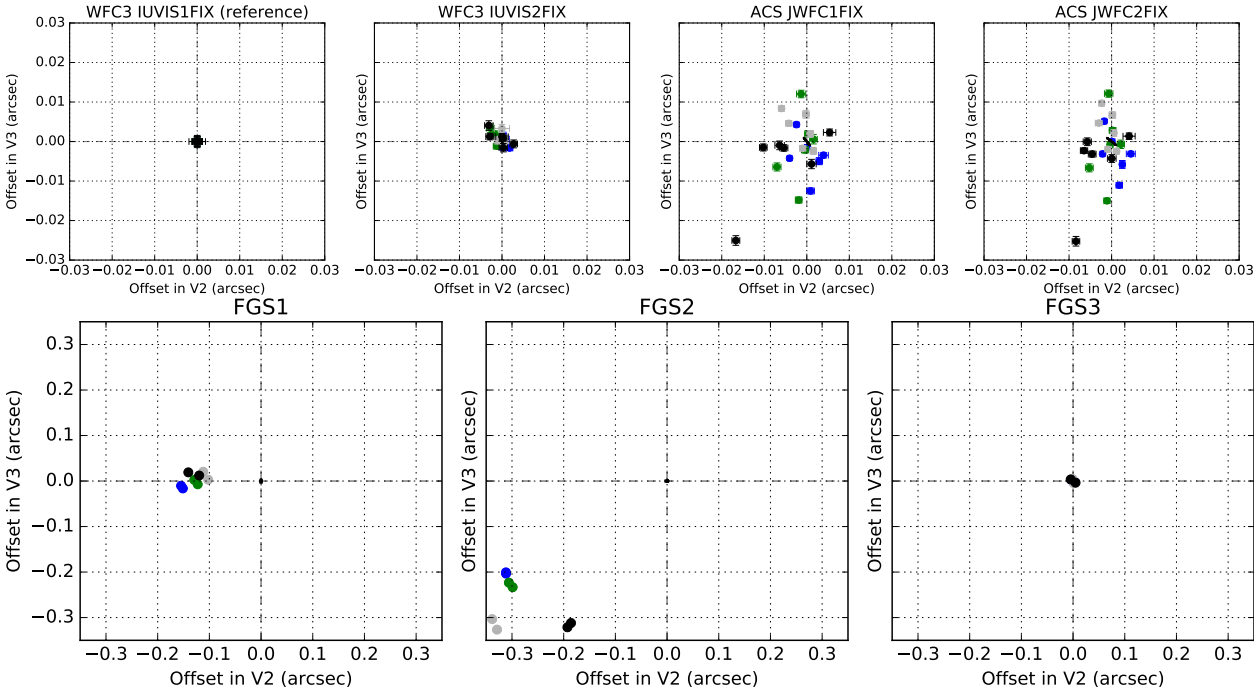

Figure 18: Results of FGS3–FGS alignment (cf. Figure 12). Since the camera aperture set as reference in this case took exposures in parallel with all other apertures, this figure (and the ones following) shows seven panels: 4 camera apertures and 3 FGS apertures. By construction, the offsets of the reference aperture are zero.

Figure 20 shows the scale offsets. The scales of FGS1 and FGS2 deviate by $\lesssim 1 \cdot 10^{-4}$ from unity, whereas we determine a scale offset for FGS3 of $\sim 7 \cdot 10^{-4}$ in V_2. The same scale offset was also determined during the FGS-SI alignment analysis and its origin is unclear. The camera scale offsets identified during the FGS-SI alignment are confirmed with additional data, which reveal no clear indication for temporal variations.

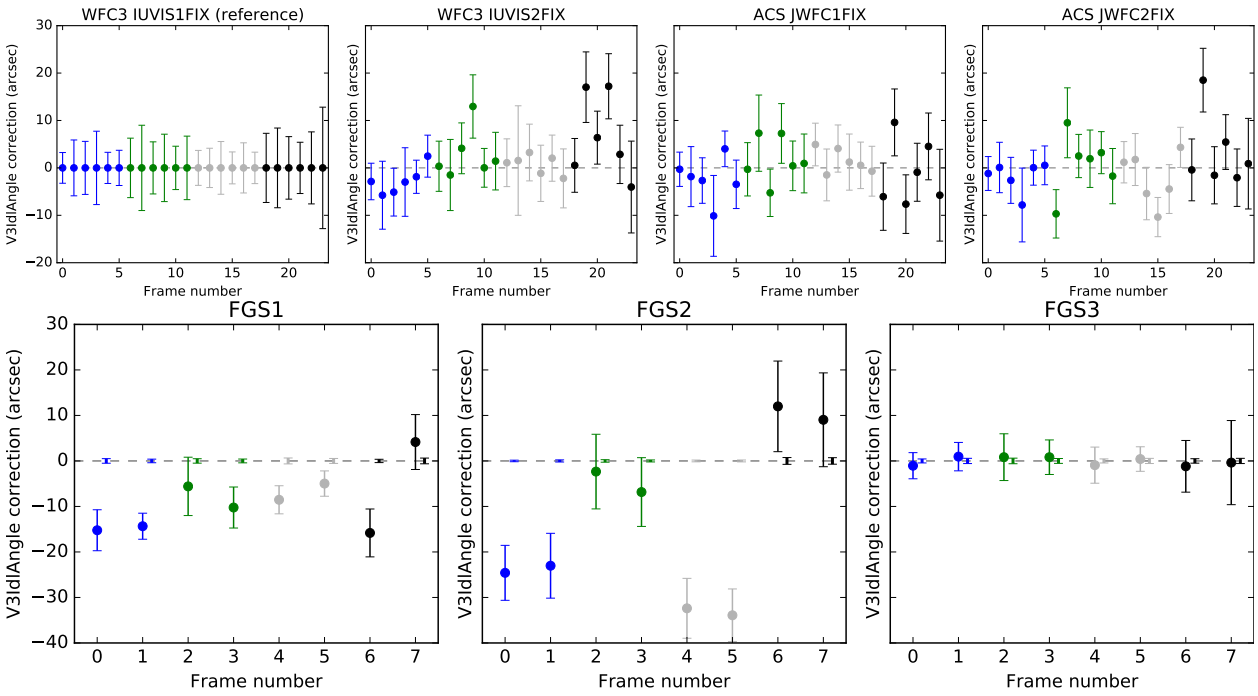

Figure 19: Results of FGS3-FGS alignment (cf. Figure 13). The angle of the reference aperture is kept fixed. For the cameras, the angle adjustment are usually consistent with zero at $1-2\sigma$ level. For FGS1 and FGS2, variations as large as $\sim 40''$ are measured.

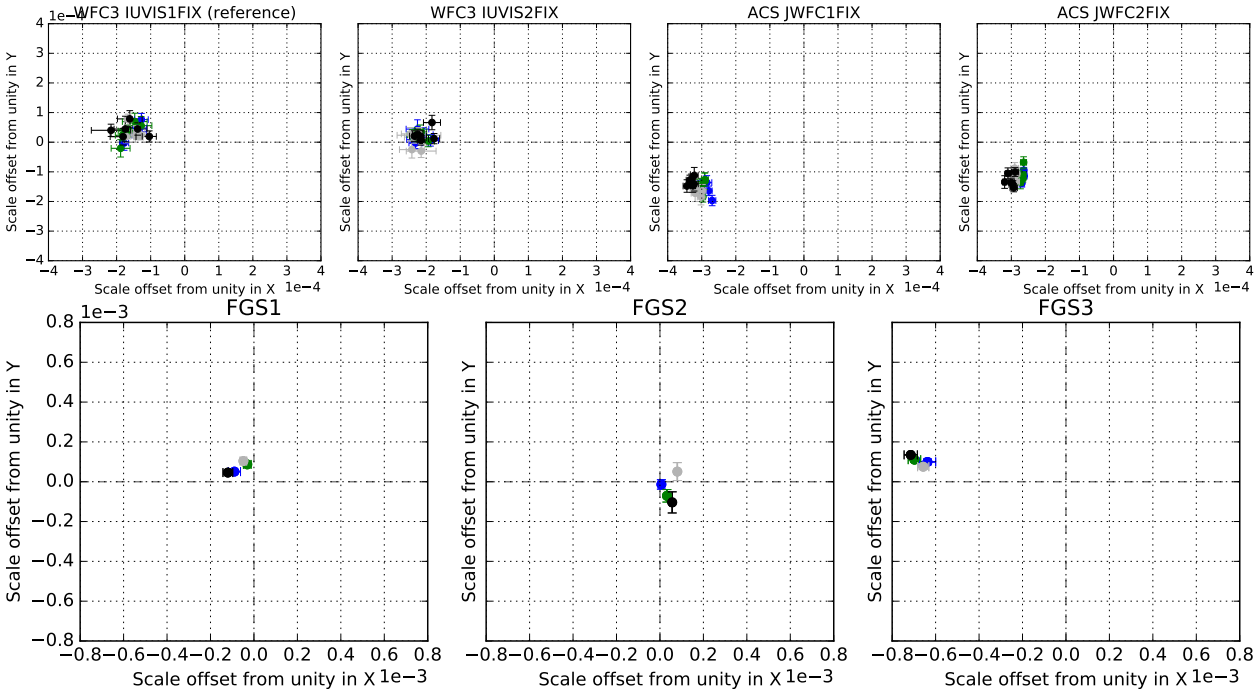

Figure 20: Results of FGS3–FGS alignment (cf. Figure 14). All camera aperture show signifiant scale offsets in V_2 direction (labelled here as 'X'), with insignificant variation. The scales of FGS1 and FGS2 are close to unity when compared to FGS3, for which we determine a scale offset in V_2 of $\sim 7 \cdot 10^{-4}$.

6.3 Refined attitude estimates

As mentioned before, the HST attitude refinement is an essential step in the alignment process. In Figure 21 we show an example of the final residuals of the attitude determination step. The residual RMS in that case is ∼6 mas for several hundred measured stars in 5 aperture. Figure 22 shows the attitude evolution as a comparison of FITS header and measured values. Tables 10 and 14 tabulate the results.

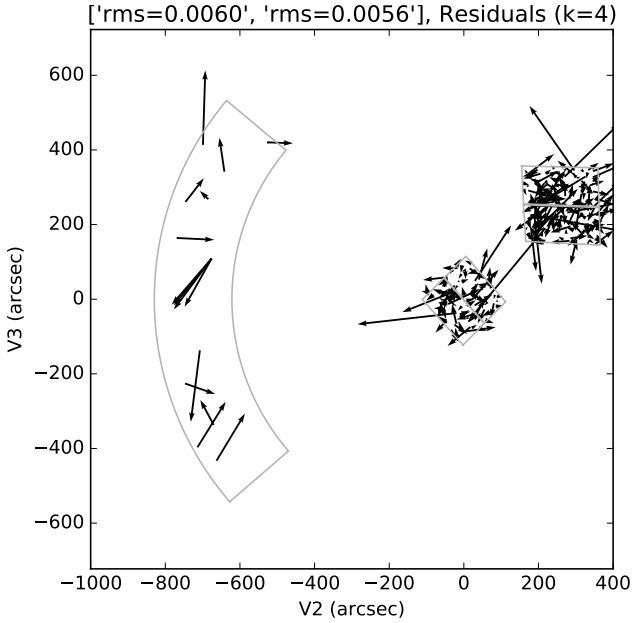

Figure 21: Residuals of the 2D polynomial fit (k=4, degree=1) at the end of the attitude determination iterative procedure, which includes adjusting the relative alignments of four apertures relative to WFC3 chip 1. The residuals for every used star are shown in the V-frame, where the V3 axis points upwards. Note that distortion is corrected at the aperture level in a previous step.

Table 10: Results of attitude determination step for the FGS–SI alignment. 'att' is the attitude group identifier, n_{ap} and $n_\star$ indicates the number of apertures and stars used, respectively. $\Delta\alpha^\star$, $\Delta\delta$, ΔPA indicate the difference of the refined attitude determination relative to RA_V1, DEC_V1, PA_V3 given in the file headers. The 'rms' column gives the residual RMS in V2 and V3.

pid_visit	date	att	n_{ap}	$n_\star$	$\Delta\alpha^\star$ (arcsec)	$\Delta\delta$ (arcsec)	ΔPA (arcsec)	rms (arcsec)
14867_13	2017-04-12	5-0	5	288	-0.3496 ± 0.0005	0.5924 ± 0.0006	20.5753 ± 0.4328	0.0060, 0.0056
14867_13	2017-04-12	5-1	5	134	-0.3478 ± 0.0006	0.5918 ± 0.0008	20.5631 ± 0.5579	0.0048, 0.0062
14867_23	2017-09-13	0-1	5	128	0.2247 ± 0.0006	-0.3181 ± 0.0006	36.5241 ± 0.5929	0.0047, 0.0044
14867_23	2017-09-13	0-0	5	260	0.2229 ± 0.0006	-0.3177 ± 0.0007	37.4556 ± 0.5367	0.0065, 0.0080
15002_13	2018-03-19	5-1	5	133	-0.2719 ± 0.0005	0.3722 ± 0.0007	37.4846 ± 0.5545	0.0045, 0.0064
15002_13	2018-03-19	5-0	5	294	-0.2744 ± 0.0004	0.3715 ± 0.0006	37.6620 ± 0.4437	0.0055, 0.0080
15002_23	2018-10-04	0-0	5	258	0.3128 ± 0.0006	-0.2814 ± 0.0005	31.3031 ± 0.4729	0.0079, 0.0075
15002_23	2018-10-04	0-1	5	129	0.3148 ± 0.0006	-0.2844 ± 0.0005	31.0018 ± 0.5236	0.0049, 0.0041

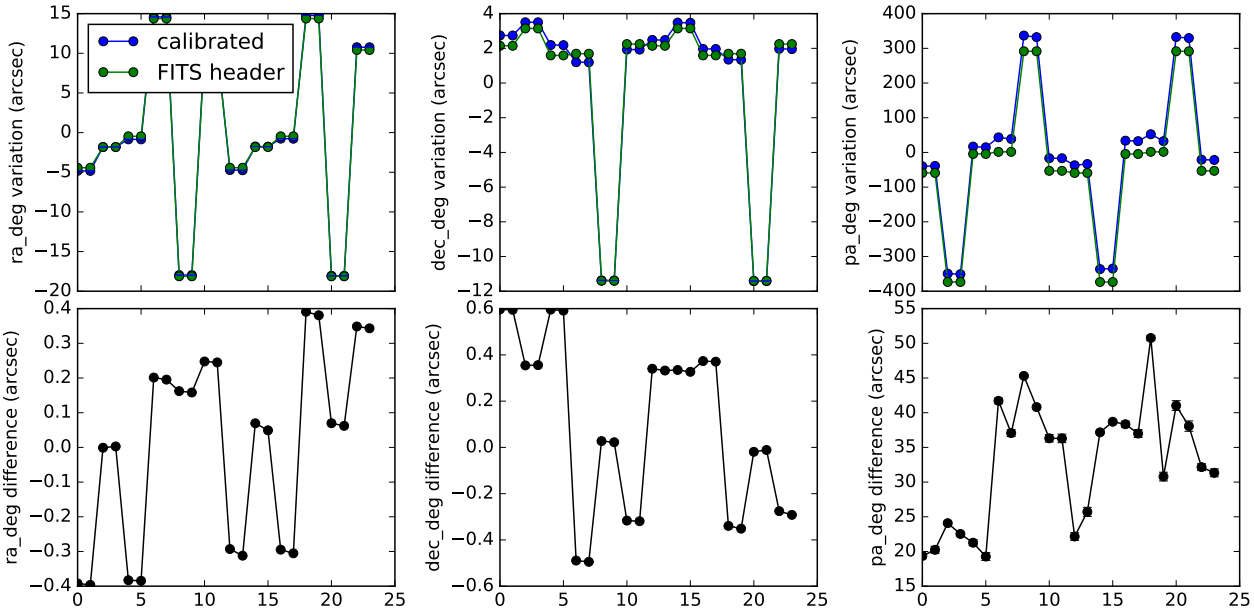

Figure 22: Comparison of attitude parameters (RA_V1, DEC_V1, PA_V3) determined in this work and given in the FITS headers. The top rows shows individual values and the bottom row shows their differences (including error bars). The x-axis shows the observation index ordered in time. Differences are typically smaller than 0.5″ in pointing and between ∼20–50″ in position angle.

6.4 Comparison with GSFC ΔV offsets determined for FGS-2R2

For comparison with an independent determination of FGS2 alignment parameters, we extracted the FGS2 TVS matrix elements from Kimmer (2019) and implemented code to extract the 'Delta V' values as tabulated in that report. We verified that our code reproduces the 'Delta V' for the 2013 data against the 2011 reference.

Table 11 shows the results. '_g' columns originate in the TVS matrices of Kimmer (2019). Since we have two sets of camera images per orbit, we report our two results in the '_s1' and '_s2' columns. When we have no data the entry is 0+/-0. Our results indicate generally larger offsets if 'Delta V2' (by ∼300 mas), whereas there is reasonable agreement in 'Delta V3'. In particular, our results reflect a similar evolution in 'Delta V3', indicating that FGS2 is drifting radially outwards in the focal plane.

Table 12 reports the same results as Table 11 but using planar approximations throughout the analysis. Considering the uncertainties, the differences are usually insignificant with some discrepancies reaching $\sim 2\sigma$.

Table 11: Comparison with GSFC results (spherical treatment). Uncertainties are derived using Monte Carlo simulations on the basis of the TVS parameter uncertainties.

date	dv1_g (mas)	dv1_s1 (mas)	dv1_s2 (mas)	dv2_g (mas)	dv2_s1 (mas)	dv2_s2 (mas)	dv3_g (mas)	dv3_s1 (mas)	dv3_s2 (mas)
2011-01	0	0 ± 0	0 ± 0	0	0 ± 0	0 ± 0	0	0 ± 0	0 ± 0
2012-12	-98	0 ± 0	0 ± 0	11	0 ± 0	0 ± 0	-573	0 ± 0	0 ± 0
2015-12	138	0 ± 0	0 ± 0	-53	0 ± 0	0 ± 0	-957	0 ± 0	0 ± 0
2017-04-12	-5	109 ± 21	104 ± 25	-29	-400 ± 2	-401 ± 2	-1088	-1031 ± 2	-1027 ± 2
2018-03-19	42	137 ± 23	142 ± 20	-45	-425 ± 2	-418 ± 2	-1191	-1134 ± 4	-1153 ± 4
2018-10-04	49	-18 ± 35	-8 ± 36	-29	-272 ± 3	-280 ± 3	-1206	-1142 ± 4	-1149 ± 4

Table 12: Comparison with GSFC results (planar approximation).

date	dv1_g (mas)	dv1_s1 (mas)	dv1_s2 (mas)	dv2_g (mas)	dv2_s1 (mas)	dv2_s2 (mas)	dv3_g (mas)	dv3_s1 (mas)	dv3_s2 (mas)
2011-01	0	0 ± 0	0 ± 0	0	0 ± 0	0 ± 0	0	0 ± 0	0 ± 0
2012-12	-98	0 ± 0	0 ± 0	11	0 ± 0	0 ± 0	-573	0 ± 0	0 ± 0
2015-12	138	0 ± 0	0 ± 0	-53	0 ± 0	0 ± 0	-957	0 ± 0	0 ± 0
2017-04-12	-5	109 ± 21	104 ± 25	-29	-394 ± 2	-394 ± 2	-1088	-1036 ± 2	-1033 ± 2
2018-03-19	42	137 ± 23	142 ± 20	-45	-421 ± 2	-412 ± 2	-1191	-1136 ± 3	-1159 ± 3
2018-10-04	49	-19 ± 35	-9 ± 36	-29	-269 ± 3	-276 ± 3	-1206	-1145 ± 4	-1155 ± 4

7 Summary and conclusions

1. We developed a rigorous model for focal plane alignment that relies on exact spherical transformations. The comparison with the results obtained using planar approximations revels that differences for HST alignment are small. We expect that the same will not be true for JWST alignments.

2. Our analysis uncovered significant scale offsets in V_2 for WFC3 ($\sim 2 \cdot 10^{-4}$), ACS ($\sim 3 \cdot 10^{-4}$), and FGS3 ($\sim 7 \cdot 10^{-4}$). The scale offset amplitudes are definitely distinct between instruments, but all offsets have the same sign. This may indicate a common origin, e.g. the use of a common astrometric catalog that imprinted its scale error in the distortion calibrations.

3. The large scale error of FGS3 is of particular concern because FGS3 defines the HST V-frame, thus all alignment results may be affected by it. We mitigated its effect on our results to some extent but we recommend the following steps to be taken:

   - Confirm the FGS3 scale offset with an independent analysis. This process is ongoing with the GSFC SAC at the time of writing.
   - Update the FGS scale and/or distortion coefficients applied in the FGS reduction pipeline (Section 4.1) and repeat the alignment analysis.

4. We determined the alignment parameters of WFC3 and ACS with formal precisions of $\sim$ 5 mas. We estimate the accuracy of our determinations to be $10 - 20$ mas. The camera aperture variations over two years are confined within $\sim$50 mas, which may indicate additional systematic errors or actual displacements. Our alignment parameters are compatible with historic determinations, but exhibit a much smaller scatter. This may reflect the significantly more accurate Gaia DR2 reference frame that was not available in the past and the quality of our comprehensive approach.

5. We determined alignment parameters of FGS2 and FGS1 relative to FGS3, which are carried in updated TVS matrix coefficients. The location of FGS1 appears stable, whereas FGS2 exhibits temporal drifts. Both findings are in qualitative agreement with independent analyses in the past. The comparison with FGS2 alignment parameters obtained independently (but with the same dataset) by the GSFC SAC, reveal common qualitative features but also significant quantitative differences, whose origins remain to be identified. However, our results confirm that FGS2 is still drifting radially outwards in the focal plane.

6. The results we obtained have not yet been verified and validated by processes established for flight products, e.g. the reprocessing of historic dataset with updated calibration products and inspecting quality indicators such as attitude residuals.

7. The dataset presented here is rich and has not yet been fully exploited. For instance, the relative motions between camera chips has not been investigated in detail.

8. One concern for future applications is that our rigorous spherical treatment may not be reflected by the operational software that applies the calibration coefficients. Care has to be taken to determine calibration parameters with the same model that is being used to apply the calibrations.

Acknowledgements

The authors would like to thank the following groups and individuals for their contributions, assistance, and advice: the GSFC SAC, in particular Ed Kimmer, Jay Anderson, Stefano Casertano, Warren Hack, Vera Kozhurina-Platais, Merle Reinhart, Randal Telfer, Maurice te Plate.

This work has made use of data from the European Space Agency (ESA) mission *Gaia* (https://www.cosmos.esa.int/gaia), processed by the *Gaia* Data Processing and Analysis Consortium (DPAC, https://www.cosmos.esa.int/web/gaia/dpac/consortium). Funding for the DPAC has been provided by national institutions, in particular the institutions participating in the *Gaia* Multilateral Agreement.

Acronyms

Gaia The Gaia astrometry mission of the European Space Agency. 1, 2, 4, 9, 16, 18, 19, 21–23, 44

pysiaf python package for handling of Science Instrument Aperture Files (SIAF) for space telescopes (https://github.com/spacetelescope/pysiaf). 1, 4, 8

fortran The fortran programming language. 1, 15, 16, 20

git Distributed version-control system. 1, 4

hst1pass HST one pass: a tool for source extraction in HST images. 1, 3, 16, 41

python The python programming language. 1, 4, 15

ACS Advanced camera for surveys (HST science instrument). 1, 13

DVA Differential velocity aberration. 1, 20

FGS Fine Guidance Sensor. 1, 4

FITS Flexible Image Transport System, a file format. 1, 16

FOV Field of view. 1, 4

GEIS Generic Edited Information Set: HST file format, similar in many ways to the FITS format standard.. 1, 15

GSFC NASA Goddard Space Flight Center. 1, 12, 13

HST Hubble Space Telescope. 1, 4

IDCTAB Instrument Distortion Correction Table. 1, 15

JWST James Webb Space Telescope. 1, 4, 9

mas milli-arcsecond. 1, 10

MAST Barbara A. Mikulski Archive for Space Telescopes. 1, 4, 15

OFAD Optical Field Angle Distortion. 1, 13, 15

OTA HST optical telescope assembly. 1, 4

POS HST FGS mode in which a star is observed in FineLock. 1, 13, 15

SAC GSFC Sensor Calibration group. 1, 13

SI Science Instrument. 1, 12–14

SIAF Science Instrument Aperture File. 1, 4, 12

SIAS HST science instrument aperture system. 1, 7

SICS HST science instrument corrected system. 1, 7

SIDS HST science instrument detector system. 1, 7

WFC3 Wide field camera 3 (HST science instrument). 1, 13

References

Abramowicz-Reed, L. 1984, Algorithms for Fine Guidance Sensor/V1. V2. V3 Alignment (Part F) and Fine Guidance Sensor/Scientific Instrument Alignment (Part 2), Tech. Rep. PR-1011, Perkin-Elmer

Anderson, J. & King, I. R. 2006, PSFs, Photometry, and Astronomy for the ACS/WFC, Tech. rep.

Blazek, H. 1984, Fine Guidance System Polarities and Coordinate Systems, Tech. Rep. PR-841, Perkin-Elmer

Bradley, A., Abramowicz-Reed, L., Story, D., Benedict, G., & Jefferys, W. 1991, PASP, 103, 317

Burrows, C. 1990, Hubble Space Telescope: Optical telescope assembly handbook. Version 1.0

Calabretta, M. R. & Greisen, E. W. 2002, A&A, 395, 1077

Cantat-Gaudin, T., Vallenari, A., Sordo, R., et al. 2018, A&A, 615, A49

Cox, C. 1997, Velocity Aberration Correction for Parallel Observations, Technical Report OSG-CAL-97-06, STScI

Cox, C. & Gilliland, R. L. 2003, in HST Calibration Workshop : Hubble after the Installation of the ACS and the NICMOS Cooling System, ed. S. Arribas, A. Koekemoer, & B. Whitmore, 58

Cox, C. & Lallo, M. 2010, in Hubble after SM4. Preparing JWST, 73

Cox, C. & Lallo, M. 2017, Description and Use of the JWST Science Instrument Aperture File, Technical Report JWST-STScI-001550, STScI

CSC/TM-82/6045. 1987, SpaceTelescope POCC Applications Software Support (PASS') Requirements Specification (Revision F), Tech. Rep. CSC/TM-82/6045, Computer Sciences Corporation

Gaia Collaboration, Brown, A. G. A., Vallenari, A., et al. 2018, A&A, 616, A1

Gaia Collaboration, Prusti, T., de Bruijne, J. H. J., et al. 2016, A&A, 595, A1

JWST-PLAN-006166. 2016, JWST Coordinate Systems Definition Document Plan, Technical Report JWST-PLAN-006166, STScI

Kennel, H. F. 1976, Space Telescope Coordinate Systems, Symbols, and Nomenclature Definitions, Tech. Rep. NASA TM X-73343, Systems Dynamics Laboratory

Kimmer, E. 2015, FGS to FGS Alignment Calibration 2015 using FALIGN Prepared Data, Tech. Rep. unpublished, GSFC

Kimmer, E. 2019, FGS-2R2 Alignment Trend, Tech. Rep. unpublished, GSFC

Luchetti, K., Abshire, G., Hallock, L., & McCutcheon, R. 1988, in Flight Mechanics/Estimation Theory Symposium 1988, ed. T. Stengle

Markley, L. & Mortari, D. 2000, AAS/AIAA Astrodynamics Specialist Conference, 103

Marrese, P. M., Marinoni, S., Fabrizio, M., & Altavilla, G. 2019, A&A, 621, A144

McArthur, B. E., Benedict, G. F., Jefferys, W. J., & Nelan, E. 2006, in The 2005 HST Calibration Workshop: Hubble After the Transition to Two-Gyro Mode, ed. A. M. Koekemoer, P. Goudfrooij, & L. L. Dressel, 396

Nelan, E. & Makidon, R. 2002, Baltimore: STScI

Price-Whelan, A. 2018, adrn/pyia: v0.3 a Python package for working with data from the Gaia mission

Sahlmann, J. 2017, Astrometric accuracy of the JWST calibration field catalog examined with the first Gaia data release, Analysis Report JWST-STScI-005492, STScI

ST/CM-07. 1984, Level II Interface Requirements Document SI to OTA & SSM, Tech. Rep. ST/CM-07, Lockheed Missiles and Space Company

A Appendix

A.1 Estimation of the hst1pass accuracy

Since hst1pass does not provide individual photocentre uncertainties, we used the residuals of the final attitude determination fit when applied to camera apertures only, to estimate empirical and magnitude-independent values. Figure 23 (left) shows the residual RMS in v2 (X) and v3 (Y) as a function of exposure time for all available 12 attitude groups. The average residual RMS is ∼4.3 mas for shallow (∼0.5 sec) exposures and ∼7 mas for deep (∼5 sec) exposures, where we averaged over both axes, both ACS and WFC3 instruments, and all extracted sources that pass the fit quality cut (Figure 5). The accuracy estimate is degraded for deep exposures, probably because more and fainter sources are extracted with larger errors in theses cases. Figure 23 (right) shows an example of the fit residuals in the V frame.

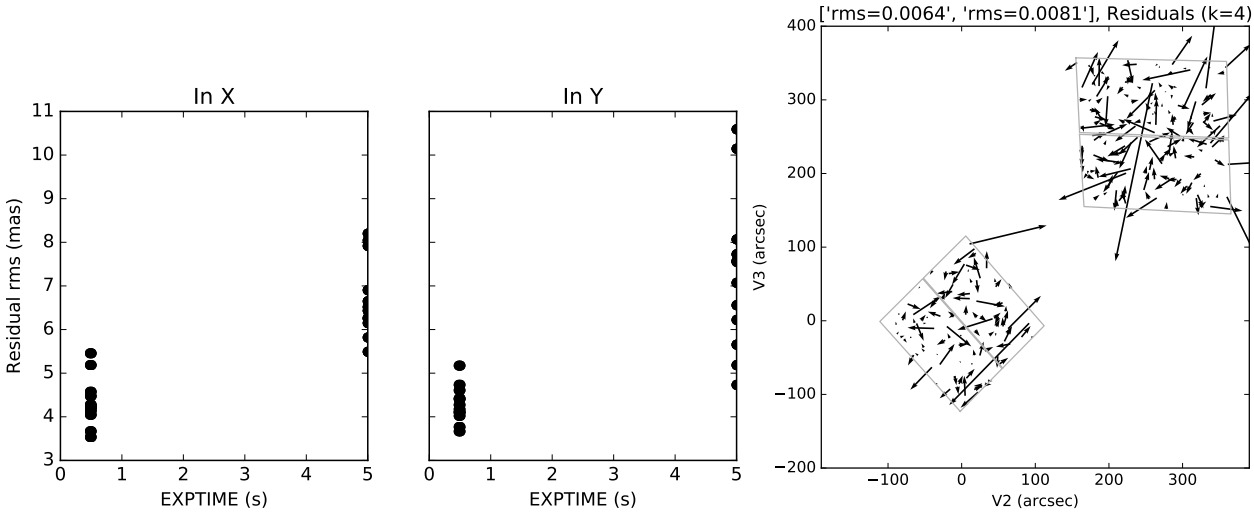

Figure 23: Estimation of the hst1pass accuracy. *Left:* Residual dispersion as function of exposure time. *Right:* Example residuals for one attitude group.

A.2 The FGS3 scale error and (some of) its consequences

One of the first surprises encountered in this work was the very significant V_2-scale discrepancy of FGS3. During the analysis and interpretation of the initial alignment results we also found surprisingly large offsets in ν_2 of up to ∼400 mas compared to the current SIAF, see Fig. 25. We show here how the latter finding was an unintended consequence of the former and how we mitigated it.

In the HST TVS formalism that we developed, the rotation angle is given around the boresight axis at $(\nu_2, \nu_3) = (0, 0)$. When computing distortion solutions, in particular as part of alignment computations, we therefore set the reference location for that transformation to the origin, i.e. to (0,0), This allowed use to translate rotation terms in the polynomial coefficients directly into corrections to the TVS angle of the concerned FGS. However, that also meant that to account for the x-scale term of $\sim 7 \cdot 10^{-4}$, the constant offset terms of the

polynomial were biased, which is directly reflected in the alignment results. At the distance of $\sim$700″, the offset introduced by the scale term is $\sim 700'' \times 7 \cdot 10^{-4} \simeq 490$ mas, which roughly matches our findings.

To circumvent this undesirable effect, we decided to use a polynomial transformation reference point at the fiducial location within the FGS aperture footprint, in exactly the same way as for the HST camera apertures. This removed the correlation between scale and offset, but means that the angle calculations do not follow the model rigorously. However, the iterative approach seems to cope well with this situation and the results with this approach appear sound. We note that these complications will not arise for JWST, because the JWST FGS apertures do not share the particular model of the HST FGS.

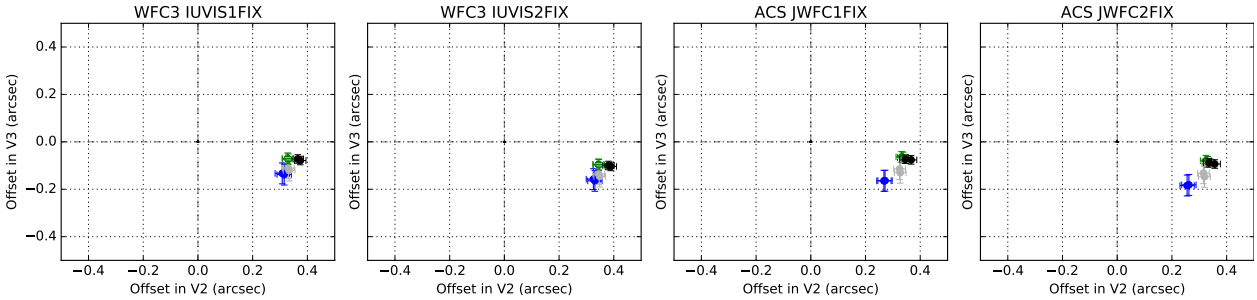

Figure 24: Results of FGS3-SI alignment before dealing with the FGS3 scale error. All apertures appear shifted by $\sim$400 mas in V_2 and ~ -100 mas in V_3.

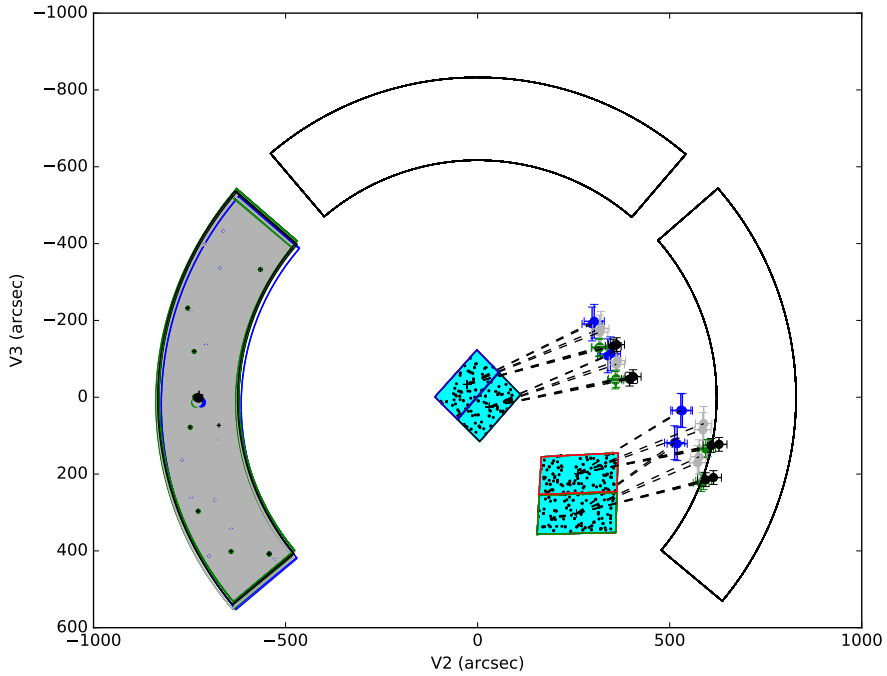

Figure 25: Results of FGS3-SI alignment before dealing with the FGS3 scale error (cf. Fig. 11).

A.3 Attitude determinations with calibrated apertures

To enable FGS–FGS alignment, our approach relies on imprinting the FGS3 alignment reference location in a camera aperture, which is then used as alignment reference for FGS1 and FGS2 in the analysis of subsequent observations. When analysing the camera data of FGS–FGS alignment runs, we noticed strong (almost linear) correlations in the apparent position of camera and FGS apertures (see e.g. the ACS apertures in Fig. 26). The orientation and amplitude of the linear structures suggested that they could be the result of attitude determination errors (in position angle). These also directly affect the FGS1 and FGS2 alignment results.

The mitigated this problem by 'freezing' the alignment of all 4 camera apertures, as determined relative to FGS3 using the 'deep' camera exposures that capture more stars, for all attitude determinations within one season. In this way, the lever arm for constraining the attitude position angle was larger and the associated errors were minimized. The ACS positions obtained in this way do not show linear structures any longer and the scatter amplitude is much reduced, see Fig. 18.

These results illustrate that, when used as attitude-determination reference, the small aperture footprints of HST camera chips combined with the moderate number of measured stars can lead to significant errors in the attitude position angle.

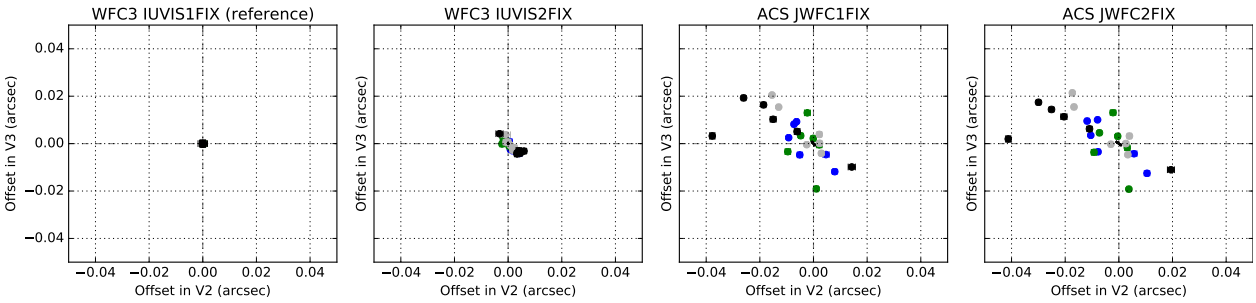

Figure 26: Results of FGS3–FGS alignment (cf. Figure 18) before 'freezing' the alignment of all 4 camera apertures for attitude determination.

A.4 Tables

Table 13: FGS target stars and their parameters from Gaia DR2, using the GSC23 cross-match table.

gsc23	*Gaia* DR2	d_{xmatch}	G	parallax	pmra	pmdec
N8CV030464	3426307862580583936	0.09	14.37	1.08	2.42	-2.73
N8CV000403	3425539299656872448	0.22	12.47	1.21	3.17	-3.43
N8CU033419	3426263018823457536	0.10	12.87	1.19	2.14	-2.87
N8CV000022	3426275010372205440	0.15	11.30	0.71	-4.25	7.05
N8CV000724	3426296214629682688	0.11	10.84	1.07	-7.10	-4.25
N8CV000713	3426297073623137152	0.09	10.51	4.64	2.71	-28.39
N8CV030082	3426297176702349952	0.14	13.25	0.87	-1.69	3.27
N8CV000699	3426297348501045248	0.06	11.73	1.95	-1.70	9.26
N8CV030100	3426295905392040320	0.03	13.50	0.46	-0.79	-0.50
N8CV029869	3426297314141311744	0.04	14.04	0.37	0.63	-2.19
N8CV030657	3426307896940735872	0.21	12.71	1.11	2.34	-2.84
N8CV000706	3426307587703095552	0.40	12.78	1.34	-0.63	-6.30
N8CV000700	3426307793861108736	0.08	12.96	1.10	2.32	-3.12
N8CV031051	3426308687214305664	0.05	14.21	0.70	5.70	-7.33
N8CV030487	3426308206177982720	0.09	13.90	2.70	5.09	-15.26
N8CV030642	3426308442400105216	0.08	13.56	2.60	-5.71	-7.08
N8CV000701	3426308377976700416	0.10	13.24	1.15	2.44	-2.80
N8CV029878	3426284841555922560	0.16	13.89	0.19	-0.18	-1.03
N8CV000710	3426307381544264064	0.83	13.11	1.15	1.51	-3.55
N8CU000116	3425514874177343360	0.03	9.31	1.11	1.80	-2.44
N8CU035919	3425514152622831872	0.10	13.66	0.40	0.83	-1.85
N8CV000478	3425538513677320192	0.04	10.87	0.36	-0.21	-3.20
N8CV023833	3425539230937537664	0.06	13.73	1.13	0.93	-13.07
N8CV026069	3426291571768270080	0.35	12.46	0.93	-0.36	0.33
N8CV025765	3426291606127995904	0.11	12.54	0.65	0.32	0.85
N8CV000819	3426290403535070848	0.19	11.28	1.02	2.04	-2.39
N8CV000766	3426292739997274880	0.02	11.93	0.62	0.66	1.13
N8CV000757	3426292946155704192	0.04	12.58	1.82	-13.24	-17.53
N8CV000767	3426292911795966848	0.09	12.51	1.19	1.60	-3.10
N8CV026739	3426291159451443456	0.17	12.99	0.64	1.49	-5.88
N8CU000181	3425513362348884992	0.12	10.47	1.19	2.24	-3.12
N8CU000189	3425511678721710592	0.02	8.65	3.38	-7.44	0.08
N8CU000184	3425511914942378752	0.05	10.17	1.16	2.58	-2.93
N8CU000166	3425512778233338112	0.03	11.82	1.11	2.37	-2.75
N8CU000172	3425512846952824960	0.08	11.31	1.17	2.25	-3.20
N8CU033101	3425512224182372608	0.06	12.29	1.25	1.65	-8.67
N8CU000180	3426263053182977408	0.12	13.40	1.57	3.08	-3.21
N8CU032509	3426257108948444288	0.03	13.29	1.13	2.50	-2.83
N8CU033324	3426257383826363904	0.07	13.22	0.44	1.07	-4.08
N8CU000175	3426258105380652160	0.08	12.98	1.28	2.63	-3.54
N8CU005016	3426258071021043200	0.83	13.24	0.29	0.27	-1.62
N8CU000194	3426257216323882880	0.12	11.03	1.10	2.80	-2.25
N8CU000150	3426258487637085312	0.02	9.93	1.09	2.54	-2.92
N8CU000196	3425511777503426432	0.14	11.62	1.15	2.24	-3.14
N8CV000765	3426284115702944384	0.03	9.74	0.96	2.46	-2.93
N8CV000340	3426285631829974528	0.10	11.17	1.30	2.69	-3.15
N8CV000779	3426282608172999552	0.17	13.39	1.09	2.33	-2.73
N8CV004953	3426281886618521728	0.19	12.82	1.14	2.38	-3.24
N8CV004590	3426281783539323776	0.14	12.52	0.05	0.51	-0.47
N8CV000404	3426280924545868544	0.41	12.18	1.12	2.37	-3.34
N8CV000419	3426280649668315776	0.03	10.06	1.24	-0.23	-2.12
N8CV000029	3426274911591681280	0.17	12.95	0.40	0.37	-1.18
N8CV000453	3426280546589109632	0.10	13.38	0.27	0.62	-1.90
N8CV000488	3426262816964116992	0.16	12.90	1.21	7.39	2.24
N8CV000491	3426262816964120320	0.10	10.41	0.67	-0.67	-4.91
N8CV000513	3426262473366746496	0.22	12.10	1.12	1.78	-3.54
N8CV000504	3426262610805859840	0.28	12.67	1.22	1.30	-6.24
N8CV000495	3426262645165423744	0.17	12.47	1.15	3.14	-2.18

Table 14: Results of attitude determination step for the FGS–FGS alignment (cf. Table 10).

pid_visit	date	att	n_{ap}	$n_\star$	$\Delta\alpha^\star$ (arcsec)	$\Delta\delta$ (arcsec)	ΔPA (arcsec)	rms (arcsec)
14867_11	2017-04-12	4-0	5	284	-0.3573 ± 0.0006	0.5968 ± 0.0006	19.3545 ± 0.3956	0.0064, 0.0065
14867_11	2017-04-12	4-1	5	128	-0.3610 ± 0.0007	0.5950 ± 0.0010	20.2380 ± 0.5049	0.0048, 0.0068
14867_12	2017-04-12	3-0	5	291	-0.0009 ± 0.0004	0.3545 ± 0.0004	24.0836 ± 0.1688	0.0063, 0.0057
14867_12	2017-04-12	3-1	5	132	0.0026 ± 0.0006	0.3558 ± 0.0005	22.5237 ± 0.2333	0.0046, 0.0046
14867_13	2017-04-12	5-0	5	288	-0.3488 ± 0.0005	0.5960 ± 0.0006	21.2636 ± 0.4376	0.0060, 0.0057
14867_13	2017-04-12	5-1	5	134	-0.3503 ± 0.0006	0.5914 ± 0.0008	19.2685 ± 0.5755	0.0050, 0.0064
14867_21	2017-09-12	1-0	5	264	0.1834 ± 0.0006	-0.4892 ± 0.0006	41.7115 ± 0.4175	0.0065, 0.0062
14867_21	2017-09-12	1-1	5	139	0.1780 ± 0.0007	-0.4948 ± 0.0007	37.0646 ± 0.4884	0.0051, 0.0054
14867_22	2017-09-12	2-0	5	281	0.1478 ± 0.0005	0.0273 ± 0.0007	45.3088 ± 0.2181	0.0063, 0.0089
14867_22	2017-09-12	2-1	5	135	0.1442 ± 0.0006	0.0223 ± 0.0006	40.8101 ± 0.2749	0.0051, 0.0053
14867_23	2017-09-13	0-0	5	260	0.2256 ± 0.0006	-0.3165 ± 0.0007	36.3098 ± 0.5353	0.0065, 0.0081
14867_23	2017-09-13	0-1	5	128	0.2232 ± 0.0006	-0.3192 ± 0.0006	36.3000 ± 0.6130	0.0049, 0.0046
15002_11	2018-03-19	4-0	5	282	-0.2669 ± 0.0007	0.3403 ± 0.0006	22.1572 ± 0.5444	0.0073, 0.0057
15002_11	2018-03-19	4-1	5	131	-0.2844 ± 0.0008	0.3323 ± 0.0007	25.7122 ± 0.6514	0.0056, 0.0049
15002_12	2018-03-19	3-0	5	285	0.0633 ± 0.0005	0.3348 ± 0.0006	37.1729 ± 0.1906	0.0065, 0.0073
15002_12	2018-03-19	3-1	5	126	0.0448 ± 0.0005	0.3268 ± 0.0008	38.6972 ± 0.2044	0.0038, 0.0057
15002_13	2018-03-19	5-0	5	294	-0.2686 ± 0.0004	0.3733 ± 0.0007	38.3382 ± 0.4465	0.0056, 0.0080
15002_13	2018-03-19	5-1	5	133	-0.2782 ± 0.0006	0.3706 ± 0.0007	36.9921 ± 0.5662	0.0046, 0.0066
15002_21	2018-10-03	1-0	5	257	0.3562 ± 0.0008	-0.3394 ± 0.0010	50.7714 ± 0.3640	0.0081, 0.0102
15002_21	2018-10-03	1-1	5	131	0.3469 ± 0.0012	-0.3514 ± 0.0016	30.7967 ± 0.6294	0.0082, 0.0102
15002_22	2018-10-04	2-0	5	278	0.0635 ± 0.0007	-0.0191 ± 0.0010	41.0228 ± 0.7152	0.0086, 0.0108
15002_22	2018-10-04	2-1	5	136	0.0566 ± 0.0007	-0.0112 ± 0.0006	38.0677 ± 0.7470	0.0069, 0.0063
15002_23	2018-10-04	0-0	5	258	0.3175 ± 0.0006	-0.2757 ± 0.0006	32.1547 ± 0.4893	0.0082, 0.0077
15002_23	2018-10-04	0-1	5	129	0.3127 ± 0.0007	-0.2917 ± 0.0005	31.3385 ± 0.5732	0.0057, 0.0043

Table 15: Our ACS alignment results compared to the current SIAF

		V2Ref (arcsec)		V3Ref (arcsec)		V3IdlYAngle (deg)	
pid_visit	AperName	SIAF	this work	SIAF	this work	SIAF	this work
14867_13	JWFC1FIX	261.647	261.4556 ± 0.0029	198.665	198.6302 ± 0.0049	177.3297	177.3246 ± 0.0009
14867_13	JWFC1FIX	261.647	261.4524 ± 0.0029	198.665	198.6283 ± 0.0049	177.3297	177.3220 ± 0.0013
14867_23	JWFC1FIX	261.647	261.4721 ± 0.0027	198.665	198.6788 ± 0.0030	177.3297	177.3246 ± 0.0013
14867_23	JWFC1FIX	261.647	261.4771 ± 0.0027	198.665	198.6767 ± 0.0031	177.3297	177.3250 ± 0.0012
15002_13	JWFC1FIX	261.647	261.4900 ± 0.0023	198.665	198.6612 ± 0.0045	177.3297	177.3249 ± 0.0010
15002_13	JWFC1FIX	261.647	261.4878 ± 0.0023	198.665	198.6760 ± 0.0045	177.3297	177.3242 ± 0.0014
15002_23	JWFC1FIX	261.647	261.4780 ± 0.0037	198.665	198.6806 ± 0.0029	177.3297	177.3276 ± 0.0014
15002_23	JWFC1FIX	261.647	261.4987 ± 0.0037	198.665	198.6776 ± 0.0029	177.3297	177.3246 ± 0.0011
14867_13	JWFC2FIX	257.378	257.1770 ± 0.0029	302.561	302.5083 ± 0.0048	177.7655	177.7598 ± 0.0009
14867_13	JWFC2FIX	257.378	257.1716 ± 0.0029	302.561	302.5047 ± 0.0049	177.7655	177.7594 ± 0.0010
14867_23	JWFC2FIX	257.378	257.1945 ± 0.0027	302.561	302.5588 ± 0.0030	177.7655	177.7615 ± 0.0010
14867_23	JWFC2FIX	257.378	257.2005 ± 0.0027	302.561	302.5541 ± 0.0030	177.7655	177.7604 ± 0.0011
15002_13	JWFC2FIX	257.378	257.2123 ± 0.0023	302.561	302.5386 ± 0.0045	177.7655	177.7597 ± 0.0011
15002_13	JWFC2FIX	257.378	257.2091 ± 0.0023	302.561	302.5539 ± 0.0045	177.7655	177.7618 ± 0.0010
15002_23	JWFC2FIX	257.378	257.2007 ± 0.0036	302.561	302.5608 ± 0.0029	177.7655	177.7586 ± 0.0009
15002_23	JWFC2FIX	257.378	257.2191 ± 0.0036	302.561	302.5559 ± 0.0029	177.7655	177.7592 ± 0.0010

Table 16: Our WFC3 alignment results compared to the current SIAF

		V2Ref (arcsec)		V3Ref (arcsec)		V3IdlYAngle (deg)	
pid_visit	AperName	SIAF	this work	SIAF	this work	SIAF	this work
14867_13	IUVIS1FIX	30.6556	30.5087 ± 0.0029	25.2168	25.2070 ± 0.0048	44.8312	44.8289 ± 0.0008
14867_13	IUVIS1FIX	30.6556	30.5018 ± 0.0029	25.2168	25.2122 ± 0.0049	44.8312	44.8271 ± 0.0009
14867_23	IUVIS1FIX	30.6556	30.4783 ± 0.0027	25.2168	25.2230 ± 0.0030	44.8312	44.8281 ± 0.0011
14867_23	IUVIS1FIX	30.6556	30.4805 ± 0.0028	25.2168	25.2192 ± 0.0031	44.8312	44.8297 ± 0.0014
15002_13	IUVIS1FIX	30.6556	30.5060 ± 0.0023	25.2168	25.2204 ± 0.0045	44.8312	44.8307 ± 0.0011
15002_13	IUVIS1FIX	30.6556	30.5031 ± 0.0023	25.2168	25.2303 ± 0.0045	44.8312	44.8282 ± 0.0008
15002_23	IUVIS1FIX	30.6556	30.5053 ± 0.0037	25.2168	25.2331 ± 0.0030	44.8312	44.8283 ± 0.0016
15002_23	IUVIS1FIX	30.6556	30.5146 ± 0.0039	25.2168	25.2262 ± 0.0029	44.8312	44.8215 ± 0.0026
14867_13	IUVIS2FIX	-27.4596	-27.5906 ± 0.0029	-33.2604	-33.2966 ± 0.0049	44.7671	44.7636 ± 0.0009
14867_13	IUVIS2FIX	-27.4596	-27.5962 ± 0.0029	-33.2604	-33.2894 ± 0.0049	44.7671	44.7642 ± 0.0011
14867_23	IUVIS2FIX	-27.4596	-27.6207 ± 0.0027	-33.2604	-33.2801 ± 0.0030	44.7671	44.7634 ± 0.0009
14867_23	IUVIS2FIX	-27.4596	-27.6190 ± 0.0027	-33.2604	-33.2828 ± 0.0030	44.7671	44.7640 ± 0.0012
15002_13	IUVIS2FIX	-27.4596	-27.5934 ± 0.0023	-33.2604	-33.2828 ± 0.0045	44.7671	44.7642 ± 0.0009
15002_13	IUVIS2FIX	-27.4596	-27.5969 ± 0.0025	-33.2604	-33.2725 ± 0.0045	44.7671	44.7627 ± 0.0016
15002_23	IUVIS2FIX	-27.4596	-27.5941 ± 0.0037	-33.2604	-33.2718 ± 0.0029	44.7671	44.7630 ± 0.0010
15002_23	IUVIS2FIX	-27.4596	-27.5849 ± 0.0037	-33.2604	-33.2760 ± 0.0029	44.7671	44.7610 ± 0.0011